Quantifying Dynamical Proxy Potential through Oceanic Teleconnections in the North Atlantic

N. Loose[1,2], P. Heimbach[1,3], H. R. Pillar[1], K. H. Nisancioglu[2,4]

[1]Oden Institute for Computational Engineering and Sciences, The University of Texas at Austin, Austin, TX, USA
[2]Department of Earth Science, University of Bergen and Bjerknes Centre for Climate Research, Bergen, Norway
[3]Jackson School of Geosciences, The University of Texas at Austin, Austin, TX, USA
[4]Department of Geosciences, University of Oslo, and Center for Earth Evolution and Dynamics, Oslo, Norway

Key Points:

- Sensitivities of key metrics, representing observed and desirable quantities in the ocean, are computed using an adjoint model
- Similar sensitivity distributions indicate proxy potential through shared ocean adjustment physics
- In contrast to conventional statistical methods, our quantification of proxy potential is rigorously dynamics-based

Corresponding author: Nora Loose, nora.loose@utexas.edu

Abstract

Oceanic quantities of interest (QoIs), e.g., ocean heat content or transports, are often inaccessible to direct observation, due to the high cost of instrument deployment and logistical challenges. Therefore, oceanographers seek proxies for undersampled, unobserved, or unobservable QoIs. Conventionally, proxy potential is assessed via statistical correlations, which measure covariability without establishing causality. This paper introduces an alternative method: assessing dynamical proxy potential. Using an adjoint model, this method unambigiously identifies the physical origins of covariability. A North Atlantic case study illustrates our method, within the ECCO (Estimating the Circulation and Climate of the Ocean) state estimate. We find that wind forcing along the eastern and northern boundaries of the Atlantic drives a basin-wide response in North Atlantic circulation and temperature. Due to these large-scale teleconnections, a single subsurface temperature observation in the Irminger Sea informs heat transport across the remote Iceland-Scotland ridge (ISR), with a dynamical proxy potential of 19%. Dynamical proxy potential allows two equivalent interpretations: Irminger Sea subsurface temperature (i) shares 19% of its adjustment physics with ISR heat transport; (ii) reduces the uncertainty in ISR heat transport by 19% (independent of the measured temperature value), if the Irminger Sea observation is added without noise to the ECCO state estimate. With its two interpretations, dynamical proxy potential is simultaneously rooted in (i) ocean dynamics and (ii) uncertainty quantification and optimal observing system design, the latter being an emerging branch in computational science. The new method may therefore foster dynamics-based, quantitative ocean observing system design in the coming years.

Plain Language Summary

To understand the Earth's changing climate, it is important to estimate how much heat the ocean takes up from the atmosphere and how the ocean recirculates the heat around the globe. Directly obtaining these estimates from measurements is complicated because oceanographers cannot measure the ocean everywhere. Ocean measurements taken from ships or freely drifting instruments are expensive and difficult to obtain, especially in regions with ice coverage or rough weather conditions. To analyze how existing measurements can be used to estimate unmeasured aspects of the ocean, past studies have used statistical correlations, although it is usually unclear whether correlations have a real, physical origin. This paper introduces a new method: we replace statistical correlations by correlations that have an underlying physical mechanism. As an example, the paper reveals that (A) a subsurface ocean temperature measurement close to the southern tip of Greenland helps to better estimate (B) poleward ocean heat transport across the Iceland-Scotland ridge, hundreds of kilometers away. (A) and (B) are related by physics-based correlation, which is created by a similar response of (A) and (B) to changes in the near- and far-field wind. The new method can be used to plan effective instrument placements in the future.

1 Introduction

Satellite altimetry and the global array of Argo floats have vastly increased the observational coverage of the world's oceans over the last two decades. Nevertheless, large parts of the ocean remain undersampled in space and time, due to the high cost of instrument deployment, ongoing technical and logistical challenges, and the fact that critically relevant processes occur on a wide range of spatial and temporal scales (e.g., Weller et al., 2019). Therefore, many oceanographic quantities of interest (QoIs) are not directly or continuously measured. Examples are volume, heat, and freshwater transports across many oceanographic passages, straits and latitude bands, as exemplified by the Atlantic meridional overturning circulation (AMOC), and ocean heat and freshwater content. Other

examples are strongly related to future societal concerns and key targets for climate predictions. These include the Niño 3.4 index, future Arctic sea ice cover, or regional sea level anomalies. In oceanography, we are therefore on the quest for proxies. That is, it is desirable - and an active part of climate research - to employ observed quantities as proxies for QoIs that are undersampled, unobserved or unobservable.

Past efforts in this direction include studies which found that sea level anomalies (available from altimetry) or ocean bottom pressure (available from gravimetry) can serve as a skillful proxy for AMOC variability on interannual time scales (e.g., Bingham & Hughes, 2009; Ezer, 2015; Frajka-Williams, 2015; Landerer et al., 2015; McCarthy et al., 2015). Other studies suggested that, on decadal and longer time scales, North Atlantic surface or subsurface temperature have a characteristic "fingerprint" associated with changes in AMOC, and that the temperature fingerprint can be used as a proxy for AMOC (e.g., Baehr et al., 2007; Caesar et al., 2018; Knight et al., 2005; Latif et al., 2004; Vellinga & Wood, 2004; R. Zhang, 2007, 2008). Consequently, sea level and surface/subsurface temperature records have been used to reconstruct AMOC changes back in time (Ezer, 2015; Frajka-Williams, 2015; Lopez et al., 2017; Ritz et al., 2013; Thornalley et al., 2018; X. Zhang et al., 2015). Moreover, sea surface height and hydrographic observations at selected locations have been proposed as a useful observing system to detect AMOC changes in the present ocean and under future climate change scenarios, complementing or substituting current direct North Atlantic trans-basin transport measurements, which are limited in space and time (see Frajka-Williams et al., 2019, for a review).

Proxy potential is typically assessed by means of statistical regression or correlation (e.g., see all AMOC proxy studies referenced in the previous paragraph), including regression using "modes" of variability obtained e.g., via principal component analysis. Fig. 1(a) sketches the concept of evaluating statistical proxy potential: one assesses covariability between an observable quantity (pink time series) and an unobserved QoI (purple time series), often in model output. This method provides an empirical measure for proxy potential, but does not identify causal relations. Without dynamical underpinnings, reported dependency on model choice, forcing scenario and time period considered (Alexander-Turner et al., 2018; Little et al., 2019; Roberts & Palmer, 2012) complicate robust identification of proxy potential. The goal of this work is to overcome the limitations of statistical proxy potential. Here, we establish a new methodology that quantifies *dynamical*, rather than statistical, proxy potential.

Our goal is to unambiguously identify shared dynamical processes and pathways that provide a mechanistic underpinning for what we will refer to as dynamical proxy potential. To do so, we take advantage of the adjoint of an ocean general circulation model. The adjoint can efficiently uncover the dynamical cause of variations in observed and unobserved ocean quantities, extracted from the equations of motion and conservation laws governing the underlying general circulation model (Marotzke et al., 1999). For instance, adjoint-derived sensitivities have been used to study the dynamical cause of the following QoIs: Atlantic meridional heat transport (Heimbach et al., 2011; Köhl, 2005; Marotzke et al., 1999), Atlantic meridional overturning circulation (Czeschel et al., 2010; Heimbach et al., 2011; Pillar et al., 2016; Smith & Heimbach, 2019), temperature in the east equatorial Pacific (Galanti et al., 2002; Galanti & Tziperman, 2003), Florida Current transport (Czeschel et al., 2012), sea level on the Californian coast (Verdy et al., 2013), ocean bottom pressure in the Arctic Mediterranean (Fukumori et al., 2015), and Labrador Sea heat content (Jones et al., 2018). Building on previous studies, we exploit the adjoint in a novel fashion, as sketched in Fig. 1(b): we identify shared mechanisms (green shading) that affect both an observed quantity (e.g., temperature in the pink box) and an unobserved QoI (e.g., heat transport across the purple section). By this approach, we find dynamical causes and controls of covariability between the observed and unobserved quantity.

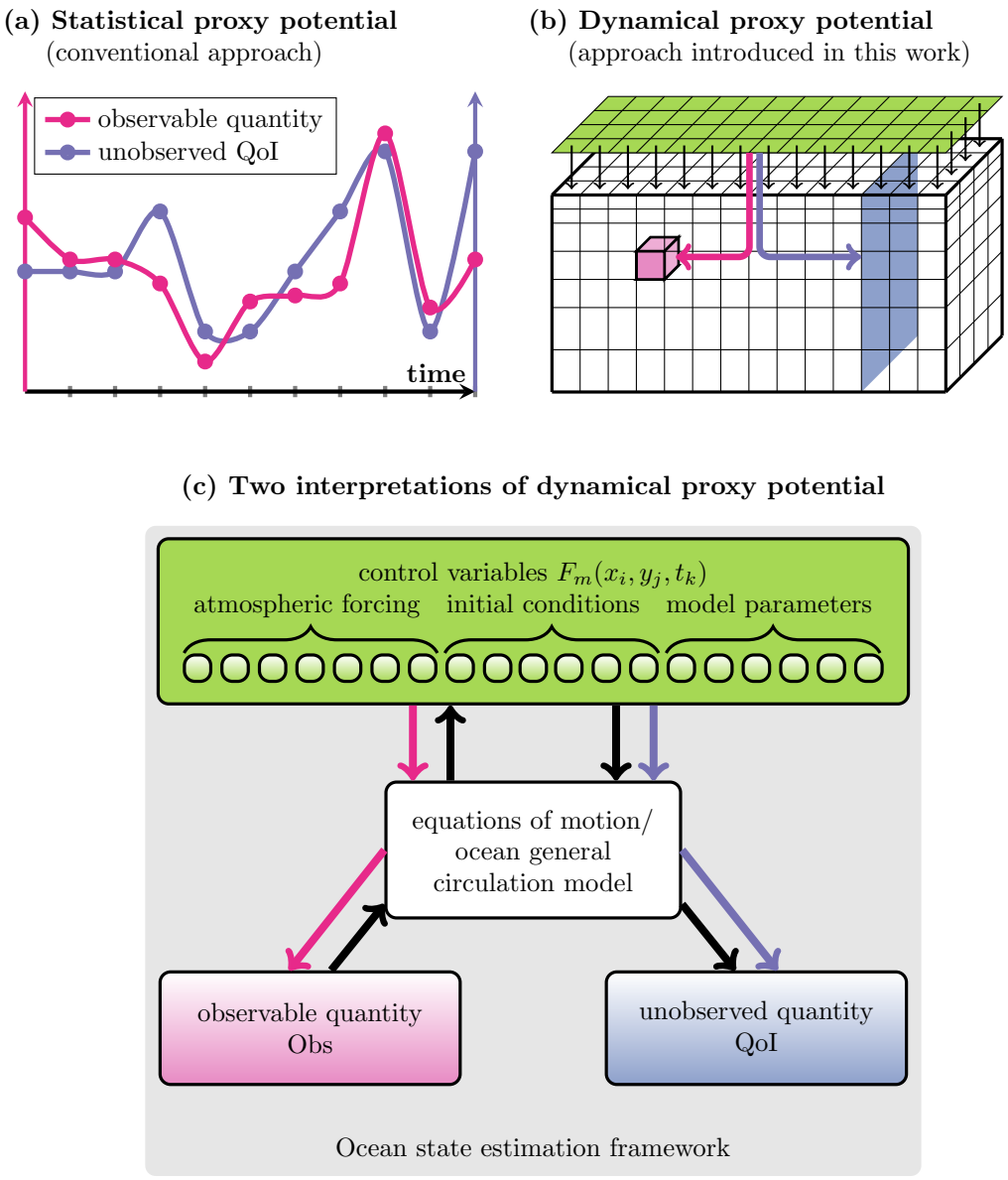

Figure 1. (a),(b) Two approaches to assess proxy potential of an observable quantity (pink) for an unobserved QoI (purple): (a) statistical proxy potential assesses covariability based on empirical evidence; (b) dynamical proxy potential assesses causes and controls (green shading) of covariability based on dynamical laws. (c) Two equivalent interpretations of dynamical proxy potential (see section 2.3): via (i) shared ocean adjustment physics (pink & purple arrows) and (ii) uncertainty quantification (black arrows).

Moreover, we establish a link between the notion of dynamical proxy potential and Hessian-based uncertainty quantification (UQ) in ocean state estimation (Tarantola, 2005; Thacker, 1989). Within the UQ framework, dynamical proxy potential can be interpreted to measure uncertainty reduction in the QoI, given the new dynamical information provided by the observation, under all potential forcing scenarios. This second interpretation of dynamical proxy potential is further developed in a forthcoming paper. The computational sciences are currently exploring UQ - or in our terminology: dynamical proxy potential - as a tool for optimal observing system design (Alexanderian et al., 2016; Bui-Thanh et al., 2012, 2013; Flath et al., 2011; Isaac et al., 2015). The novel approach introduced in this work may therefore contribute to foster UQ and optimal observing system design in the field of ocean climate science in the coming years.

We illustrate the new concept of dynamical proxy potential for a case study in the North Atlantic, choosing heat transport across the Iceland-Scotland ridge as our exemplary QoI. The Iceland-Scotland ridge (ISR) is the key gateway for poleward heat progession from the North Atlantic toward the Arctic Ocean (Hansen & Østerhus, 2000). Warm Atlantic waters are carried across the ridge by the Norwegian Atlantic Current (NwAC), one of the main branches of the North Atlantic Current (NAC, see Fig. 2). While observational estimates for ISR heat transport since the mid 1990s exist (e.g., Berx et al., 2013; Hansen et al., 2015; Østerhus et al., 2005, 2019), cross-ridge heat transport estimates remain uncertain, due to a sparse array of current meter moorings and the sensitivity to the choice of calculation method (Berx et al., 2013; McCarthy et al., 2019). In contrast, upper ocean temperatures are well constrained throughout the larger part of the North Atlantic basin via remote and in situ platforms. For this reason, we select our representative observed quantities as temperature at the sea surface and at 300 m depth, at two locations in the North Atlantic: in the Irminger Current (IC) and off the Portuguese coast (Fig. 2), monitored by the OSNAP (Lozier et al., 2017, 2019) and OVIDE (Lherminier et al., 2007; Mercier et al., 2015) sections, respectively. These locations are intentionally chosen in two branches of the NAC that are distinct from the branch crossing the ISR (Fig. 2) and are therefore not expected to be ideal placements for monitoring ISR heat transport. We will show that these observations nevertheless provide partial constraints on the QoI through shared adjustment physics, which are uncovered and quantified by dynamical proxy potential.

Here, we work within the ECCO (Estimating the Circulation and Climate of the Ocean) version 4 state estimate (Forget et al., 2015) and focus on monthly to multiannual time scales up to five years, since now approximately five years of continuous OSNAP measurements are available. We note that the quantification of dynamical proxy potential does not require actual (here: OSNAP and OVIDE) observational data, since it investigates dynamical relationships in the model equations, rather than observed covariability. This paper is structured as follows. In section 2, we introduce the framework of ocean state estimation, describe the inbuilt adjoint infrastructure, and explain how these tools are used to compute dynamical proxy potential. Section 3 applies the methodology to our North Atlantic case study. In section 4, we discuss our results as well as limitations and future directions.

2 Assessing Dynamical Proxy Potential

To assess dynamical proxy potential, we leverage the framework of ocean state estimation and inbuilt adjoint capability. Ocean state estimation defines a set of uncertain input or control variables (green box in Fig. 1(c)). For simplicity, we will refer to the control variables as the time-dependent two-dimensional forcing fields $F_m(x_i, y_j, t_k)$. In practice, control variables also comprise time-independent three-dimensional fields of initial conditions and model parameters. In ocean state estimation, each forcing variable $F_m(x_i, y_j, t_k)$ gets assigned a weight, $\Delta F_m(x_i, y_j, t_k)$, reflecting an estimate of the forcing uncertainty. Ocean state estimation then fits the model to the available obser-

vations. For this, one adjusts the control variables, within the range of their weights. In contrast, the model state variables within the white box in Fig. 1(c), e.g., temperature and velocity, adjust freely following the model dynamics, to ensure dynamic and kinematic consistency. An implicit assumption in ocean state estimation is that the control variables $F_m(x_i, y_j, t_k)$ comprise all possible sources of changes in the ocean state and circulation and that the model is perfect (Tarantola, 2005; Wunsch, 1996).

2.1 Information Required vs. Information Captured

Given a quantity of interest, QoI, and an observed quantity, Obs, we compute their linear sensitivity to all forcings $F_m(x_i, y_j, t_k)$, using the adjoint of the underlying general circulation model. The weighted sensitivity matrices

$$\tilde{\mathbf{Q}} = \left[\frac{\partial(\text{QoI})}{\partial F_m(x_i, y_j, t_k)} \Delta F_m(x_i, y_j, t_k)\right]_{i,j,k,m} \tag{1}$$

and

$$\tilde{\mathbf{V}} = \left[\frac{\partial(\text{Obs})}{\partial F_m(x_i, y_j, t_k)} \Delta F_m(x_i, y_j, t_k)\right]_{i,j,k,m} \tag{2}$$

reveal all possible dynamical mechanisms via which typical perturbations in the forcing fields $F_m(x_i, y_j, t_k)$ can change the QoI and observed quantity, respectively. All the different dynamical mechanisms encoded in $\tilde{\mathbf{Q}}$ have to be informed by the observations; $\tilde{\mathbf{Q}}$ is therefore the information required to recover the QoI. Similarly, $\tilde{\mathbf{V}}$ is the information captured by the observed quantity.

2.2 Quantifying the Constraint Provided

Comparing the sensitivity distributions of the QoI and observed quantity, identifies the adjustment physics that affect both quantities. A comparison of sensitivities is rigorously performed by the following three consecutive steps:

1. normalizing the weighted sensitivity matrices $\tilde{\mathbf{Q}}$ and $\tilde{\mathbf{V}}$ via the respective normalization factor

$$\sigma_{\text{Quantity}} = \sqrt{\sum_{i,j,k,m} \left(\frac{\partial(\text{Quantity})}{\partial F_m(x_i, y_j, t_k)} \cdot \Delta F_m(x_i, y_j, t_k)\right)^2}, \tag{3}$$

   for Quantity $\in \{\text{QoI}, \text{Obs}\}$, resulting in

$$\mathbf{Q} = \sigma_{\text{QoI}}^{-1}\, \tilde{\mathbf{Q}}, \qquad \mathbf{V} = \sigma_{\text{Obs}}^{-1}\, \tilde{\mathbf{V}}, \tag{4}$$

2. projecting $\mathbf{Q}$ onto $\mathbf{V}$, and
3. taking the square of this projection.

These three steps result in the dynamical proxy potential of the observed quantity for the QoI:

$$(\mathbf{Q} \bullet \mathbf{V})^2 = \left((\sigma_{\text{QoI}} \cdot \sigma_{\text{Obs}})^{-1} \sum_{i,j,k,m} \left\{ \left[\frac{\partial(\text{QoI})}{\partial F_m(x_i, y_j, t_k)} \cdot \Delta F_m(x_i, y_j, t_k)\right] \cdot \left[\frac{\partial(\text{Obs})}{\partial F_m(x_i, y_j, t_k)} \cdot \Delta F_m(x_i, y_j, t_k)\right] \right\} \right)^2. \tag{5}$$

The projection in eq. (5) compares the information required, $\mathbf{Q}$, with the information captured, $\mathbf{V}$. The square of this projection provides the dynamical proxy potential, ranging between 0 and 1. These bounds correspond to the cases for which Obs (0) provides

no constraint and (1) serves as a *perfect* proxy for the QoI. The expression in eq. (5) is valid for measuring the dynamical proxy potential of a *single* observation for the QoI. This expression can be generalized for multiple available observations, through an orthogonalization of the observations' sensitivity matrices, as will be the demonstrated in forthcoming work.

2.3 Two Equivalent Interpretations

The concept of dynamical proxy potential, as defined in eq. (5), has two equivalent interpretations, sketched in Fig. 1(c). Dynamical proxy potential of an observed quantity (pink box) for an unobserved QoI (purple box) measures

(i) the similarity between the ocean adjustment physics for the observed vs. unobserved quantity (pink vs. purple arrows) in response to changes in forcing (green box), on a scale from 0% (*no similarity*) to 100% (*identical*);
(ii) the relative uncertainty reduction in the QoI that would be achieved if the observation were to be added without noise to the state estimation framework in Fig. 1(c). The flow of information and uncertainty reduction within the state estimation framework - from the observation via the controls to the QoI - is delineated by the black arrows in Fig. 1(c).

Interpretation (i) provides the following intution: if the observed quantity and QoI are forced by similar ocean mechanisms and pathways, the observed quantity can capture a large degree of the variability of the QoI, thus has high dynamical proxy potential for the QoI. Interpretation (ii) is formally derived in the supporting information and will be more thoroughly explained in a forthcoming paper, while this paper mainly focuses on enlightening interpretation (i).

3 Application to the North Atlantic

This section exemplifies our method for a case study in the North Atlantic. Section 3.1 describes the experimental setup, including our choice of QoI and observations. Sections 3.2 and 3.3 present the information required to recover the QoI and the information captured by the observations, respectively. Section 3.4 assesses the dynamical proxy potential of the observations for the QoI.

3.1 Experimental Setup

Our experiments are performed about the ECCO version 4 release 2 (ECCOv4r2, Forget et al., 2015) solution. The Massachusetts Institute of Technology general circulation model (MITgcm, J. Marshall, Adcroft, et al., 1997; J. Marshall, Hill, et al., 1997), serves as the dynamical core in ECCO and is configured at a nominal horizontal resolution of 1° with 50 vertical levels in this release. The optimized state provides an acceptable fit to most available oceanographic data and has been used extensively for mechanistic investigations of ocean variability, including in the North Atlantic (e.g., Buckley et al., 2014; Jones et al., 2018). We refer the reader to Forget et al. (2015) for details on the model configuration and estimated ocean state.

To quantify dynamical proxy potential, one requires the linear sensitivities of the QoI and observed quantities to all forcing variables (eqs. (1),(2)). To perform these sensitivity calculations, we take advantage of the flexible ECCOv4 adjoint modeling framework (Forget et al., 2015). Algorithmic differentiation, through source-to-source code transformation with the commercial tool transformation of algorithms in Fortran (TAF Giering & Kaminski, 1998), produces the code for our adjoint models. Ice-covered regions are masked in the sensitivity calculation.

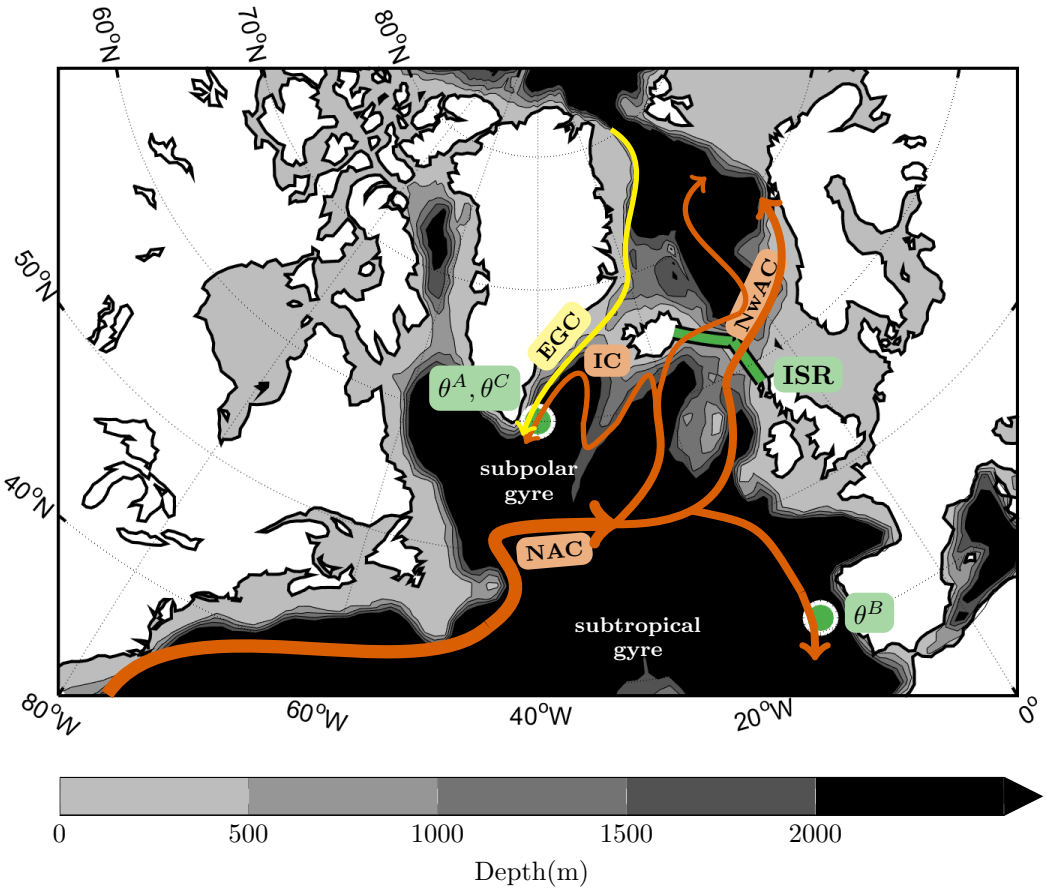

Figure 2. Schematic of the North Atlantic quantities examined in our case study. The quantity of interest (QoI) is heat transport across the Iceland-Scotland ridge (ISR, green line). The temperature observations θ^A, θ^B and θ^C are located inside the green dots. θ^A and θ^B are subsurface (at 300 m depth), θ^C at the sea surface. The arrows represent approximate pathways of major near-surface currents carrying warm, saline Atlantic waters (orange) and cold, fresh Arctic waters (yellow): NAC = North Atlantic Current; NwAC = Norwegian Atlantic Current; IC = Irminger Current; EGC = East Greenland Current.

3.1.1 QoI and Observations

The QoI in our case study is heat transport across the Iceland-Scotland ridge, denoted by $\mathrm{HT_{ISR}}$. We investigate three different temperature observations in the North Atlantic, located inside the green dots in Fig. 2 and labelled by θ^A, θ^B, and θ^C. Observations θ^A and θ^C are located in the Irminger Sea at $(40\,^\circ\mathrm{W}, 60\,^\circ\mathrm{N})$, while observation θ^B is situated in the eastern North Atlantic off the Portuguese coast at $(12\,^\circ\mathrm{W}, 41\,^\circ\mathrm{N})$. θ^A and θ^B are subsurface observations, situated at 300 m depth, and θ^C is a surface observation.

We quantify the dynamical proxy potential of the five-year mean of the observations for the five-year mean of our QoI, for zero lag. Sensitivity matrices of the QoI (eq. (1)) and observations (eq. (2)) are computed from the final five years (2007-2011) of the ECCOv4r2 state estimate. Dependence of the specific evaluation period is weak, given that $\mathrm{HT_{ISR}}$, θ^A, θ^B, and θ^C depend approximately linear on the forcing variables in Table 1 (Appendix A).

The QoI, as simulated by the model, is diagnosed as follows:

$$\mathrm{HT_{ISR}} = \frac{\rho_0\, c_p}{\Delta t} \int_{2007}^{2011} \int_{\mathrm{bottom}}^{\mathrm{top}} \int_L (\theta - \theta_{\mathrm{ref}})\, v^\perp \, dL\, dz\, dt \quad [\mathrm{W}]. \tag{6}$$

L denotes the Iceland-Faroe-Scotland line segment, $\Delta t = \int_{2007}^{2011} dt$ the length of the integration period, $\rho_0 = 1029\,\mathrm{kg/m^3}$ the reference density, and $c_p = 3994\,\mathrm{J/(kg \cdot K)}$ the specific heat capacity of water. Further, θ denotes potential temperature, and $v^\perp$ the velocity perpendicular to the line segment L; sign convention is such that positive $v^\perp$ corresponds to positive north- and eastward velocity. Note that since L is only a partial line segment, rather than a closed boundary, heat transport in equation (6) has to be defined relative to a reference temperature θ_{ref} (Schauer & Beszczynska-Möller, 2009). Consistent with many observational studies (e.g., Østerhus et al., 2005; Berx et al., 2013; Hansen et al., 2015), we choose $\theta_{\mathrm{ref}} = 0\,^\circ\mathrm{C}$, motivated by the observation that southward flow across the ISR is close to this temperature (Hansen et al., 2003).

For $\star \in \{A, B, C\}$, the observation θ^* is diagnosed as the mean potential temperature

$$\theta^\star = \frac{1}{\Delta t \cdot \mathcal{V}^\star} \int_{2007}^{2011} \int_{h_0^\star}^{h_1^\star} \int_{\mathcal{A}^\star} \theta \, dx\, dy\, dz\, dt \quad [^\circ\mathrm{C}]. \tag{7}$$

$(h_0)^\star$, $(h_1)^\star$, and $\mathcal{A}^\star$ denote the lower and upper boundaries, and the horizontal area, of the model grid cell which the respective observation $\theta^\star$ is located in. For the subsurface observations ($\star = A, B$), we have $(h_0)^\star = -325\,\mathrm{m}$ and $(h_1)^\star = -275\,\mathrm{m}$. For the surface observation, we choose the uppermost two model grid cells as a representative depth range, corresponding to $(h_0)^C = -20\,\mathrm{m}$ and $(h_1)^C = 0\,\mathrm{m}$. The area of $\mathcal{A}^A = \mathcal{A}^C$ is approximately $(52\,\mathrm{km})^2$ and the area of $\mathcal{A}^B$ is approximately $(84\,\mathrm{km})^2$. In equation (7), θ denotes potential temperature, $\Delta t = \int_{2007}^{2011} dt$ the length of the integration period and $\mathcal{V}^\star = \int_{h_0^*}^{h_1^*} \int_{\mathcal{A}^*} dx\, dy\, dz$ the volume of interest.

3.1.2 Forcings and Weights

Table 1 shows the set of forcing fields that is chosen in this work: the spatially-varying fields of net upward surface heat flux, $Q_{\mathrm{net},\uparrow}$, net surface freshwater flux, E-P-R, and zonal and meridional wind stress, τ_x and τ_y, respectively. Consistent with assessing dynamical proxy potential of the five-year mean of the observations for the five-year mean of the QoI, only adjustments to changes in the five-year mean of the forcing fields are considered (fourth column in Table 1).

The weights associated with the forcing fields are set to the spatially constant values shown in the last column of Table 1. Choosing the weights as spatially uniform im-

Table 1. Forcing Fields and Weights in our Case Study.

m	Forcing $F_m(x_i, y_j, \bar{t})$	Symbol	Time average	ΔF_m
1	Net upward surface heat flux	$Q_{\text{net},\uparrow}$	five years	$50\,\text{W/m}^2$
2	Net surface freshwater flux	E-P-R	five years	$5 \cdot 10^{-8}\,\text{m/s}$
3	Zonal wind stress	τ_x	five years	$0.05\,\text{N/m}^2$
4	Meridional wind stress	τ_y	five years	$0.05\,\text{N/m}^2$

plies that the sensitivity projection (eq. (5)) for each individual forcing field is fully determined by the adjustment physics, and not by the forcing weight. In contrast, spatially varying weights can obscure the relative importance of sensitivity/physics vs. weights (Pillar et al., 2018). The choice of uniform weights adds therefore clarity to the presentation in this paper, whose primary goal is to exemplify the new concept of dynamical proxy potential. The concept of dynamical proxy potential permits straightforward generalization to spatially (and even temporally) varying weights as per eq. (5).

3.2 Information Required to Recover the QoI

Figs. 3(a)-(d) show the weighted and normalized sensitivities

$$\mathbf{Q}_{.,.,m} = \sigma_{\text{HT}}^{-1} \left[\frac{\partial(\text{HT}_{\text{ISR}})}{\partial F_m(x_i, y_j, \bar{t})} \Delta F_m \right]_{i,j}, \qquad m = 1, 2, 3, 4, \tag{8}$$

equal to the information required to recover HT_{ISR} (cf. eqs. (1),(4)). Here, $\bar{t}$ indicates that we consider five-year mean sensitivities, and ΔF_m are the uniform forcing weights from Table 1. The normalization factor, $\sigma_{\text{HT}} = 11\,\text{TW}$, is computed according to eq. (3). The bar chart in Fig. 3(e) shows the relative importance of the four forcings F_m for impacting HT_{ISR}. Relative importance is measured by the ratios

$$\|\mathbf{Q}_{.,.,m}\|^2 = \sigma_{\text{HT}}^{-2} \sum_{i,j} \left(\frac{\partial(\text{HT}_{\text{ISR}})}{\partial F_m(x_i, y_j, \bar{t})} \Delta F_m \right)^2, \qquad m = 1, 2, 3, 4, \tag{9}$$

equivalent to integrating the sensitivities in Fig. 3(a)-(d) around the globe (in the l^2-norm). Fig. 3(e) demonstrates that the influence of wind stress, τ_x and τ_y, prevails over the influence of buoyancy forcing, $Q_{\text{net},\uparrow}$ and E-P-R.

The positive sensitivity of HT_{ISR} to τ_y along the western African and European coast (Fig. 3(d)) is consistent with the following dynamical mechanism. An increase in northward wind stress along the western African and European coast induces Ekman onshore convergence and a positive pressure anomaly along the coast. The positive pressure anomaly travels northward, along the eastern boundary of the North Atlantic, to the eastern end of the ISR. The increased zonal pressure gradient leads to a strengthened northward geostrophic transport across the ridge, and, consequently, an increase in HT_{ISR}. The sensitivity to zonal wind stress along the western African and European coastline (Fig. 3(c)) is due to the same mechanism. Here, the sensitivity sign alternates because it is determined by the orientation of the coastline.

The emerging wind stress sensitivities of HT_{ISR} around Iceland (Figs. 3(c),(d)) can be explained by a similar mechanism. The Icelandic coastline is a waveguide for clockwise propagation around Iceland, delivering signals to the western end of the ISR section. Thus, negative pressure anomalies along the entire Icelandic coastline result in a positive perturbation of the zonal pressure gradient along the ISR section, and a strengthening of the northward geostrophic transport across the ridge. This explains the sign of the sensitivities around Iceland: increased eastward (westward) wind stress along the southern (northern) coast of Iceland (Fig. 3(c)) and increased southward wind stress along the

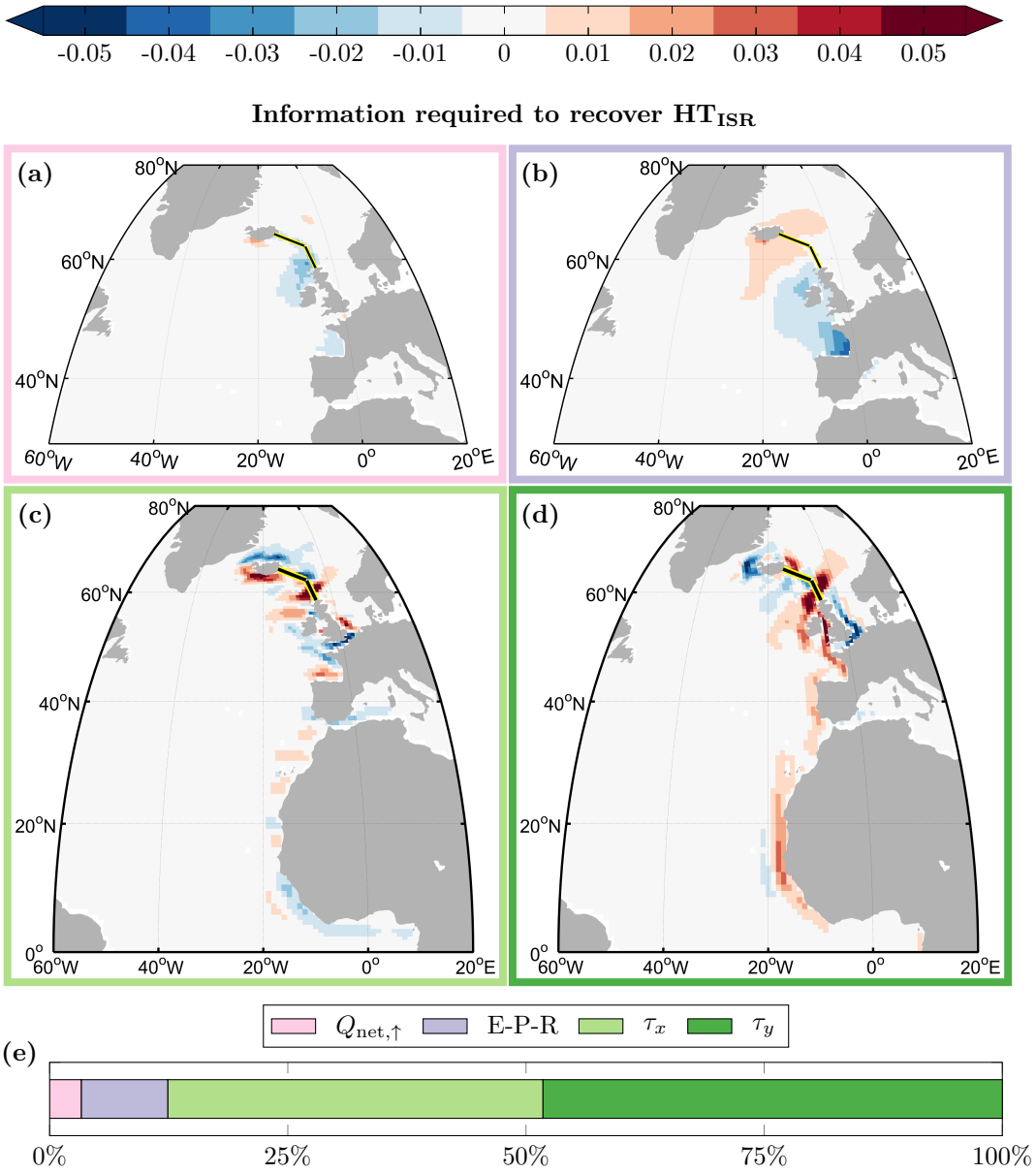

Figure 3. Sensitivities of five-year mean heat transport across the Iceland-Scotland ridge (HT_{ISR}), to changes in the five-year mean (a) upward surface heat flux $Q_{net,\uparrow}$, (b) surface freshwater flux E-P-R, (c) zonal wind stress τ_x and (d) meridional wind stress τ_y. The sensitivities are weighted and normalized (eq. (8)). Red (blue) colors indicate that an increase in (a) heat loss to the atmosphere, (b) surface salinification, (c) eastward wind stress and (b) northward wind stress would lead to a subsequent increase (decrease) in HT_{ISR} on a five-year time scale. The solid black-yellow contour in (a)-(d) delineates the ISR. The bar chart in (e) shows the relative contributions of $Q_{net,\uparrow}$, E-P-R, τ_x and τ_y to HT_{ISR} sensitivity, when integrating the sensitivities in (a)-(d) around the globe (eq. (9)).

western coast of Iceland (Fig. 3(d)), all drive Ekman offshore divergence, resulting in a negative pressure anomaly at the Icelandic coast and a subsequent increase in $\mathrm{HT}_{\mathrm{ISR}}$. The wind stress sensitivity dipole along the coastline of the United Kingdom (UK) seen in Figs. 3(c),(d) can be understood similarly. The responsible mechanism delivers positive pressure anomalies to the eastern end of the ISR section, explaining the fact that the sensitivity dipoles around Iceland and the UK are of opposite sign.

$\mathrm{HT}_{\mathrm{ISR}}$ shows positive sensitivity to $Q_{\mathrm{net},\uparrow}$ and E-P-R to the west of the ISR, around Iceland, and negative sensitivity to the east of the ISR, along the western European coast (Figs. 3(a),(b)). This sensitivity dipole across the core of the NAC is consistent with a strengthening of the cross-ridge geostrophic transport in response to a negative perturbation of the density gradient along the section. The sensitivity of $\mathrm{HT}_{\mathrm{ISR}}$ to $Q_{\mathrm{net},\uparrow}$, relative to the remaining forcing fields, is surprisingly small: only 3% (Fig. 3(e)). We note that even if we tripled ΔQ_{net} in Table 1, while keeping the weights for the remaining forcings unchanged, $\mathrm{HT}_{\mathrm{ISR}}$ would still be less sensitive to $Q_{\mathrm{net},\uparrow}$ than to any of the remaining three forcing fields in Fig. 3(e). This is consistent with previous observation- and model-based studies, which found that on seasonal to multiannual time scales ISR heat transport variability is dominantly driven by velocity fluctuations, rather than temperature fluctuations (Årthun & Eldevik, 2016; Asbjørnsen et al., 2019; Orvik & Skagseth, 2005).

3.3 Information Captured by Observations

The information captured by each of the three temperature observations $\theta^\star$, for $\star = A, B, C$, is represented by the weighted and normalized sensitivities

$$\mathbf{V}^\star_{\cdot,\cdot,m} = \sigma_\star^{-1} \left[\frac{\partial \theta^\star}{\partial F_m(x_i, y_j, \bar{t})} \Delta F_m \right]_{i,j}, \qquad m = 1, 2, 3, 4, \tag{10}$$

cf. eqs. (2),(4). Here, the normalization factor $\sigma_\star$ is computed according to eq. (3) with Quantity $= \theta^\star$, giving $\sigma_A = 0.05\,^\circ\mathrm{C}$, $\sigma_B = 0.06\,^\circ\mathrm{C}$, and $\sigma_C = 0.23\,^\circ\mathrm{C}$. Note that σ_C is much larger than σ_A and σ_B since the surface temperature θ^C is more sensitive to atmospheric forcing than the subsurface temperatures θ^A, θ^B. Figs. 4(a)-(f) show the weighted and normalized sensitivities (eq. (10)) for two of the four forcings, $F_1 = Q_{\mathrm{net},\uparrow}$ and $F_4 = \tau_y$. The bar charts in Figs. 4(g)-(i) show the relative importance of the four forcings F_m for impacting $\theta^\star$, for $\star = A, B, C$. Relative importance is measured as in Fig. 4(d), by the ratios in eq. (9), where $\mathbf{Q}$ is substitued by $\mathbf{V}^\star$.

The relative importance of $Q_{\mathrm{net},\uparrow}$ is high for the surface observation θ^C (Fig. 4(i)), but low for the subsurface observations θ^A and θ^B (Figs. 4(g),(h)). The high sensitivity of θ^C to $Q_{\mathrm{net},\uparrow}$ is concentrated at the observed site (Fig. 4(c)), due to the strong influence of local air-sea heat fluxes on surface temperature. All temperature observations show weak negative $Q_{\mathrm{net},\uparrow}$ sensitivity upstream of the respective observed sites (Figs. 4(a)-(c)), as an increased upward heat flux locally cools surface waters which are then advected (Fig. 2) to the observed locations. For all three temperature observations, the relative importance of E-P-R is very small (Figs. 4(g)-(i)). Wind stress is important for all three observations (Figs. 4(g)-(i)), and the remainder of this section is devoted to wind stress sensitivities. For the sake of brevity, we focus on τ_y sensitivities, which can be regarded as representative for τ_x sensitivities, too. Indeed, τ_x and τ_y sensitivities emerge along the same pathways (not shown) due to the same wind-driven adjustment mechanisms.

All observations are characterized by a sensitivity dipole local to the observed site and explained by Ekman dynamics. For instance, at $(12\,^\circ\mathrm{W}, 41\,^\circ\mathrm{N})$, right where θ^B is located, a sensitivity dipole is visible, with positive sensitivities to the west and negative sensitivities to the east (Fig. 4(e)), interrupting the otherwise positive sensitivities along the eastern boundary of the Atlantic. Here, a wind stress perturbation matching the sensitivity dipole (i.e., increased northward wind stress to the west and increased southward wind stress to the east) causes Ekman downwelling and pumps warm surface waters down to the subsurface observation, which increases θ^B.

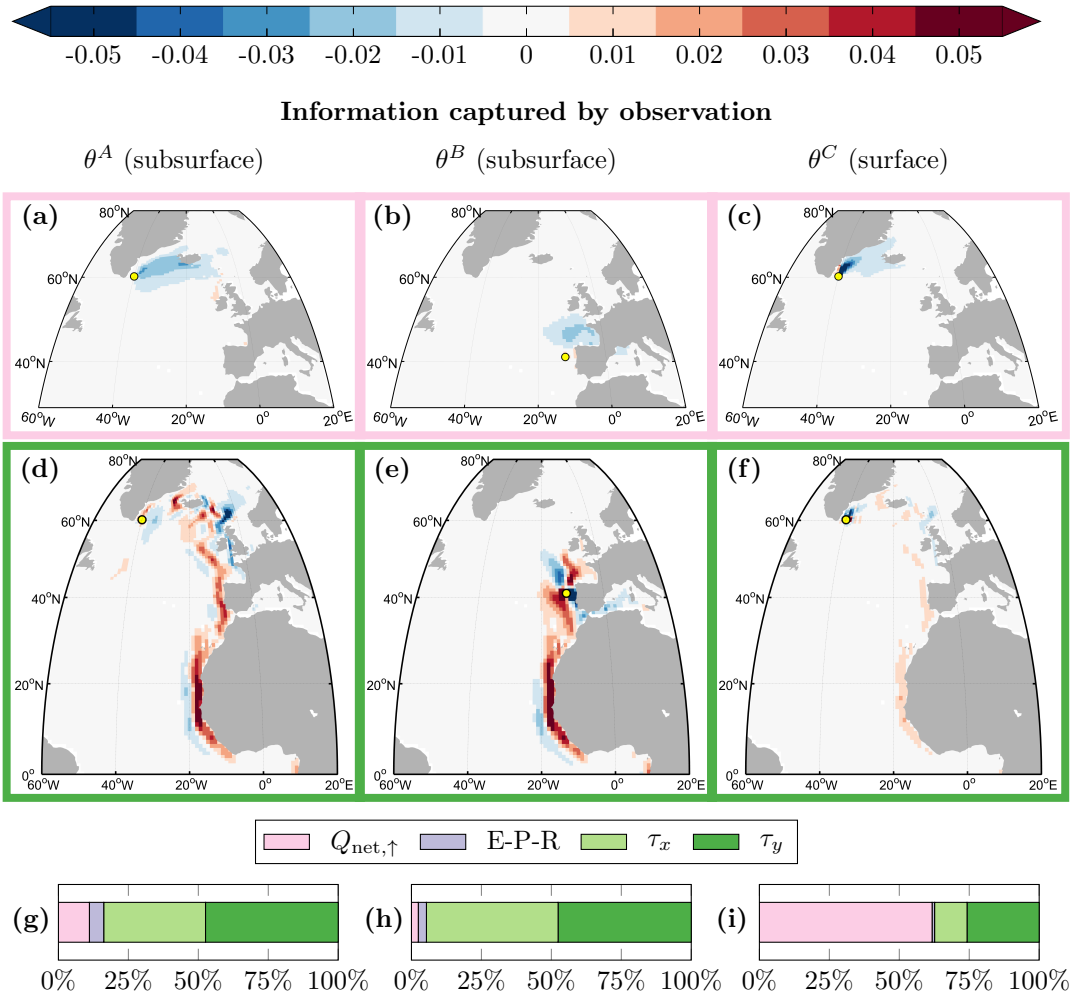

Figure 4. (a)-(c): Sensitivities of five-year mean (a) subsurface temperature in the Irminger Sea (θ^A), (b) subsurface temperature off the Portuguese coast (θ^B), and (c) surface temperature in the Irminger Sea (θ^C) to changes in five-year mean upward surface heat flux $Q_{\mathrm{net},\uparrow}$. (d)-(f): Same as (a)-(c), but sensitivities to meridional wind stress τ_y. The sensitivities are weighted and normalized (eq. (10)), as in Fig. 3. Red (blue) colors indicate that an increase in (a),(b),(c) heat loss to the atmosphere and (d),(e),(f) northward wind stress would lead to a subsequent increase (decrease) in (a),(d) θ^A, (b),(e) θ^B, and (c),(f) θ^C on a five-year time scale. The yellow dots mark the respective locations of the temperature observation. The bar charts in (g)-(i) show the relative contributions of $Q_{\mathrm{net},\uparrow}$, E-P-R, τ_x and τ_y to (g) θ^A, (h) θ^B, and (i) θ^C sensitivity, computed as in Fig. 3.

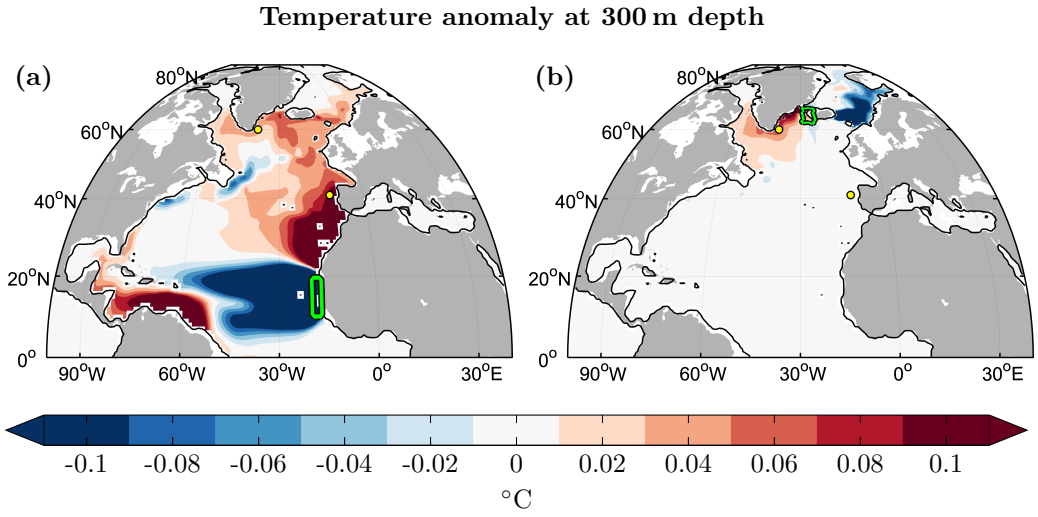

Figure 5. Response of North Atlantic subsurface temperature at 300 m depth to a positive northward wind stress anomaly of amplitude $0.05\,\mathrm{N/m^2}$ along the (a) western African coast and (b) the western Icelandic coast. The wind stress perturbations are imposed inside the green contour in (a) and (b), and maintained over five years. The shown temperature anomalies are time-averaged over the same five-year time period. The black line marks the 300 m depth contour. The yellow dots show the locations of the temperature observations θ^A and θ^B.

The large-scale wind stress sensitivity patterns of θ^C (Fig. 4(f)) are very similar to the ones of θ^A (Fig. 4(d)), except that they are of much weaker amplitude. The similarity of the patterns suggests that the surface observation θ^C is sensitive to similar remote wind-driven adjustment mechanisms as the subsurface observations θ^A. However, local forcing massively dominates the surface temperature response, as indicated by the strong sensitivities concentrated near $(40\,^\circ\mathrm{W}, 60\,^\circ\mathrm{N})$ in Figs. 4(c),(f).

For all three temperature observations, positive sensitivity to northward wind stress emerges along the western African and European coastline (Figs. 4(d)-(f)), similar to what was seen for $\mathrm{HT_{ISR}}$ in section 3.2. To explain the underlying mechanism, we perform a perturbation experiment, in which the final five years of the ECCOv4r2 serve as our control simulation. We increase northward wind stress in the region highlighted in Fig. 5(a), along the western African coast, by $0.05\,\mathrm{N/m^2}$, and maintain the perturbation over the full five-year period. Fig. 5(a) shows the response anomalies in subsurface temperature, at a depth of 300 m, time-averaged over the five-year experiment. We see that, in response to the positive northward wind stress anomaly along the western African coast, the northeast Atlantic (north of $30\,^\circ\mathrm{N}$) experiences anomalous high temperatures.

The responsible mechanism operates exactly as demonstrated by Jones et al. (2018), see their Fig. 10. The northward wind stress anomaly creates a positve pressure anomaly along the eastern boundary of the Atlantic, which, after traveling across the ISR, sets up an anomalous pressure gradient between the Nordic Seas and the North Atlantic. The basin-scale pressure gradient along the eastern and northern boundary of the North Atlantic spins up the subpolar gyre and the northeastern part of the subtropical gyre. The strengthened subpolar and subtropical gyres lead to the large-scale subsurface warming pattern that is seen in the northeast Atlantic in Fig. 5(a). The anomalous warming includes the locations of the temperature observations θ^A, θ^B, and θ^C, in the Irminger Sea and off the Portuguese coast, explaining the consistently positive sensitivities along the western African coast in Figs. 4(d)-(f). We also note that the positive temperature anomaly

in the Norwegian Sea in Fig. 5(a) is a consequence of increased $\mathrm{HT_{ISR}}$, as predicted by the positive τ_y sensitivity band along the western African coast in Fig. 3(d).

North of 50 °N, the subsurface temperature observation off the Portuguese coast, θ^B, is insensitive to wind stress (Figs. 4(e)). Meanwhile, the temperature observations in the Irminger Sea show sensitivity to wind stress also in the northeastern Atlantic, between 50 °N and 70 °N (Figs. 4(d),(f)). We note that, in this region, the pattern of τ_y sensitivities for θ^A, θ^C (Figs. 4(d),(f)) are comparable to those for $\mathrm{HT_{ISR}}$ (Fig. 3(d)), except that sensitivities of θ^A, θ^C are of opposite sign, compared to $\mathrm{HT_{ISR}}$ (see Figs. 6(c),(d) for a side-by-side comparison).

To explain the opposite signs, we perform a second perturbation experiment similar to the one presented in Fig. 5(a). In the second experiment, we increase northward wind stress along the western Icelandic coast, in the region highlighted in Fig. 5(b), where θ^A and θ^B show positive sensitivity (Fig. 4(d),(f)) and $\mathrm{HT_{ISR}}$ shows negative sensitivity (Fig. 3(d)). Fig. 5(b) shows the response anomaly in subsurface temperature, at a depth of 300 m. The Irminger and Labrador Seas experience a warming, while the Norwegian Sea cools. The underlying mechanism is the following: the northward wind stress anomaly along the western Icelandic coast drives Ekman onshore convergence and a positive pressure anomaly. The positive pressure anomaly is rapidly communicated along the entire Icelandic coastline, resulting in an across-bathymetry pressure gradient, which drives an anomalous clockwise barotropic circulation around Iceland (not shown). The anomalous clockwise circulation around Iceland weakens the northward transport across the ISR by the NwAC as well as the southward transport through Denmark Strait by the East Greenland Current (EGC), while strengthening the IC (cf. Fig. 2). The weakened northward transport of warm Atlantic waters across the ISR leads to the anomalous cold temperatures that are seen in the Norwegian Sea in Fig. 5(b), and is consistent with a reduced $\mathrm{HT_{ISR}}$, as predicted by the *negative* sensitivities in Fig. 3(d). The weakened southward transport of cold Arctic waters through Denmark Strait, together with the strengthened IC, results in the anomalous warming that is seen in the Irminger and Labrador Seas in Fig. 5(b). The increased temperature in the Irminger Sea is consistent with the *positive* sensitivities along the western Icelandic coast in Figs. 4(d),(f).

The perturbation experiment presented in Fig. 5(b) explains the opposite sign in the sensitivities along the western Icelandic coast in Fig. 3(d) vs. Fig. 4(d). The fact that in Fig. 3(d) vs. Fig. 4(d), sensitivities are *consistently* of opposite sign in the northeast Atlantic between 50 °N and 70 °N can be understood similarly. The sensitivity patterns in this region are characterized by topographically steered bands, which connect to Iceland or the ISR (Figs. 3(d), 4(d)). The sensitivity patterns have opposite sign in Fig. 3(d) vs. Fig. 4(d) because wind stress in this region creates pressure anomalies that are transported to the Icelandic coastline. Once there, the pressure anomalies drive a simultaneous strengthening (or weakening) of the NwAC and EGC, as described before, which results in opposite temperature responses in the Irminger vs. Norwegian Sea, similarly as in Fig. 5(b).

3.4 Quantifying the Constraint Provided

This section investigates the contraints on our QoI, heat transport across the Iceland-Scotland ridge ($\mathrm{HT_{ISR}}$), provided by the three temperature observations θ^A, θ^B, and θ^C. These constraints are quantified by dynamical proxy potential, computed as the square of the following projection of sensitivity matrices:

$$\mathbf{Q} \bullet \mathbf{V}^\star = \left[\sigma_{\mathrm{HT}}^{-1} \frac{\partial(\mathrm{HT_{ISR}})}{\partial F} \Delta F\right] \bullet \left[\sigma_\star^{-1} \frac{\partial \theta^\star}{\partial F} \Delta F\right], \tag{11}$$

for $\star = A, B, C$, cf. eq. (5). Fig. 6 shows the projection (11) for the case $\star = A$. The left column of Fig. 6 shows the information that is required to recover $\mathrm{HT_{ISR}}$. The right column of Fig. 6 contains the information that is captured by the temperature obser-

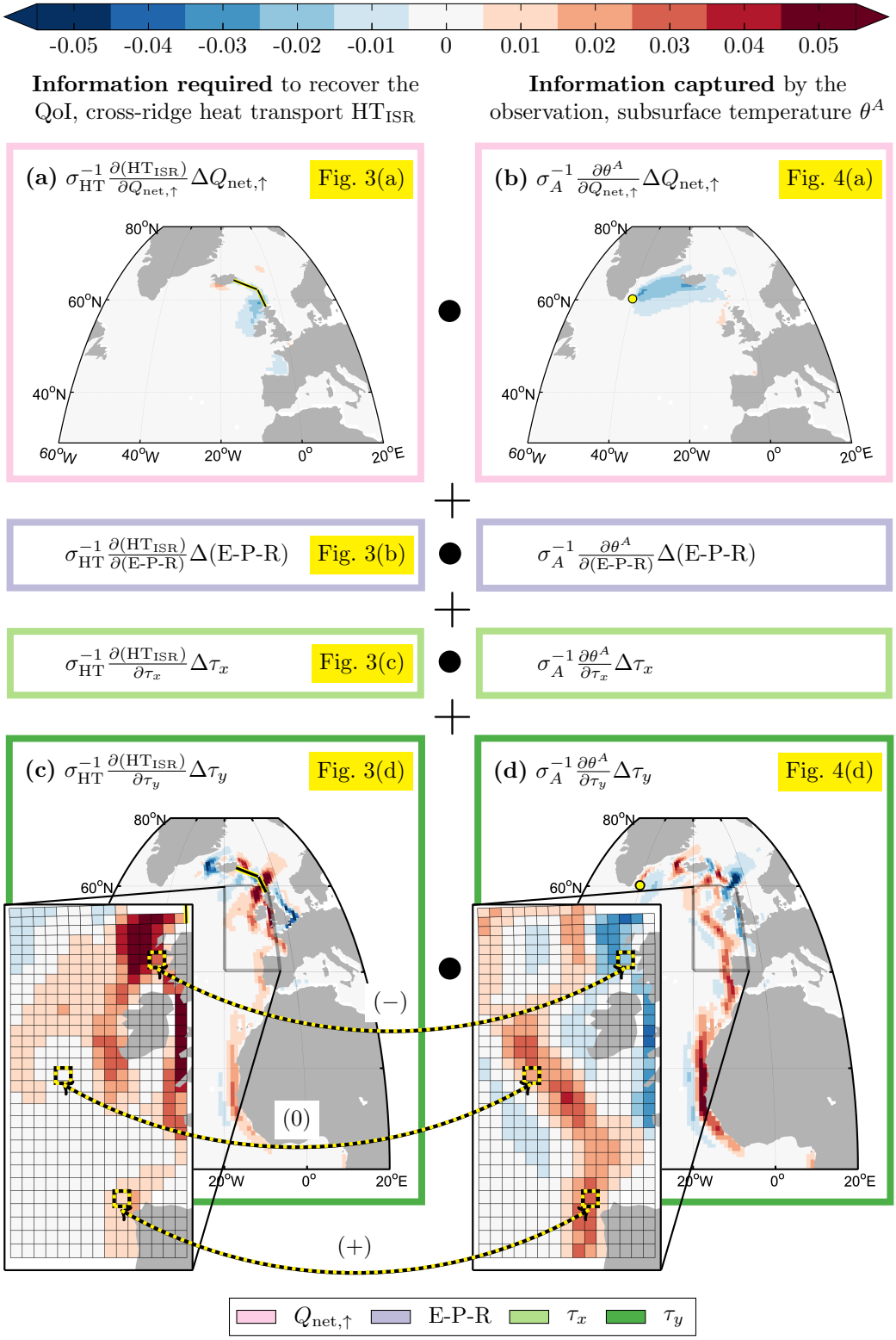

Figure 6. Projection of sensitivity matrices (eq. (11)) of the QoI, $\mathrm{HT}_{\mathrm{ISR}}$ (left column), and the observed quantity, θ^A (right column). All shown sensitivity maps are replots of subpanels in Fig. 3 and 4, as indicated by the yellow labels. The color shading in each of the shown model grid cells (inlets in (c),(d)) corresponds to an entry in either of the two sensitivity matrices, associated with the forcing variable τ_y. The three cases (+), (−), and (0), resulting from the elementwise projection, are further discussed in the text.

vation θ^A. In Fig. 6(c)-(d), we highlight three cases resulting from the elementwise projection in eq. (11):

(+) overlapping sensitivities of equal sign, resulting in a *positive* contribution to the projection $\mathbf{Q} \bullet \mathbf{V}^A$;
(−) overlapping sensitivities of opposite sign, resulting in a *negative* contribution to $\mathbf{Q} \bullet \mathbf{V}^A$;
(0) non-overlapping sensitivities, resulting in *no* contribution to $\mathbf{Q} \bullet \mathbf{V}^A$.

Fig. 7(i) is a quantitative summary of Fig. 6: showing total positive (case (+)) and negative (case (−)) contributions to the projection $\mathbf{Q}\bullet\mathbf{V}^A$, for the four different forcings. The maximum absolute value for the projection is equal to 1, because the sensitivity matrices in (11) are normalized. An absolute value of 1 would only be attained if the sensitivity matrices of $\mathrm{HT_{ISR}}$ and θ^A, $\mathbf{Q}$ and $\mathbf{V}^A$, were identical, or identical with reversed sign.

For all observations considered, the generation of proxy potential is dominated by existence of wind-driven adjustments that are shared with those for $\mathrm{HT_{ISR}}$ (Figs. 7(i)-(k)). Minor importance of $Q_{\mathrm{net},\uparrow}$ and E-P-R is not surprising when recalling the fact that $\mathrm{HT_{ISR}}$ is relative insensitive to $Q_{\mathrm{net},\uparrow}$ and E-P-R (Fig. 7(a)). Note that even for the surface temperature observation θ^C, which is highly sensitive to surface heat fluxes (Fig. 7(d)), the $Q_{\mathrm{net},\uparrow}$ contribution to the projection (11) is negligible (Fig. 7(k)).

Positive τ_y contributions to $\mathbf{Q} \bullet \mathbf{V}^A$ arise along the eastern boundary of the Atlantic (solid box, Fig. 7(f)), where both $\mathrm{HT_{ISR}}$ and θ^A exhibit a band of positive sensitivity along the western African and European coast, due to the shared pressure adjustment mechanism discussed in sections 3.2, 3.3 and Fig. 5(a). Negative τ_y contributions to $\mathbf{Q}\bullet\mathbf{V}^A$ arise in the northeast Atlantic (dashed box, Fig. 7(f)), where wind stress sensitivities are of large amplitude and of opposite sign for $\mathrm{HT_{ISR}}$ (Fig. 7(e)) and θ^A (Fig. 7(f)), as discussed in section 3.3 and Fig. 5(b). The negative projection in the northeast Atlantic exceeds the positive projection in the eastern Atlantic waveguide (Fig. 7(i)). Total positive and negative contributions sum to $\mathbf{Q}\bullet\mathbf{V}^A = -0.44$ (Fig. 7(i)). Here, partial cancellation between the positive and negative projections leads to a loss of constraint by $c^A = 0.29$. For $\star = A, B, C$, cancellation is quantified as

$$c^\star = |\mathbf{Q}| \bullet |\mathbf{V}^\star| - |\mathbf{Q} \bullet \mathbf{V}^\star| \geq 0, \tag{12}$$

where $|\mathbf{M}|$ denotes the matrix whose entries are defined as the absolute values of the respective entries of the matrix $\mathbf{M}$, for $\mathbf{M} = \mathbf{Q}, \mathbf{V}^\star$. As an example, if all contributions shown in Fig. 7(i) were either consistently positive or consistently negative (in which cases no cancellation occurred), the absolute value of the projection $\mathbf{Q}\bullet\mathbf{V}^A$ would be increased by the addition of c^A, resulting in an absolute value of $0.44 + 0.29 = 0.73$.

Positive wind stress contributions to $\mathbf{Q}\bullet\mathbf{V}^B$ (Fig. 7(j)) are of similar magnitude as positive wind stress contributions to $\mathbf{Q}\bullet\mathbf{V}^A$ (Fig. 7(i)), due to the pressure adjustment mechanism in the eastern Atlantic waveguide, shared among θ^B, $\mathrm{HT_{ISR}}$ (and θ^A). The total overlap of $\mathrm{HT_{ISR}}$ sensitivity with θ^B sensitivity (Fig. 7(j)) is much smaller than with θ^A sensitivity (Fig. 7(i)), since θ^B does not show any sensitivity north of 55 °N (Fig. 7(g)). For the Irminger Sea surface observation θ^C, proxy origins are similar as for the Irminger Sea subsurface observation θ^A (boxes in Figs. 7(f),(h)), but contributions from each forcing are reduced by a factor of about 0.25 (Figs. 7(i),(k)), due to relatively weaker excitation of surface temperature by remote forcing, as discussed in section 3.3.

The dynamical proxy potential of each of the observations θ^A, θ^B, and θ^C for $\mathrm{HT_{ISR}}$ is computed by taking the square of the respective value $\mathbf{Q}\bullet\mathbf{V}^\star$ (eq. (5)) that was obtained in Figs. 7(i)-(k). The result is shown in Figs. 7(l)-(n): the dynamical proxy potential of θ^A for $\mathrm{HT_{ISR}}$ is 19%, while the dynamical proxy potentials of θ^B and θ^C for $\mathrm{HT_{ISR}}$ are only 1%. These values can be interpreted either in terms of (i) shared ocean

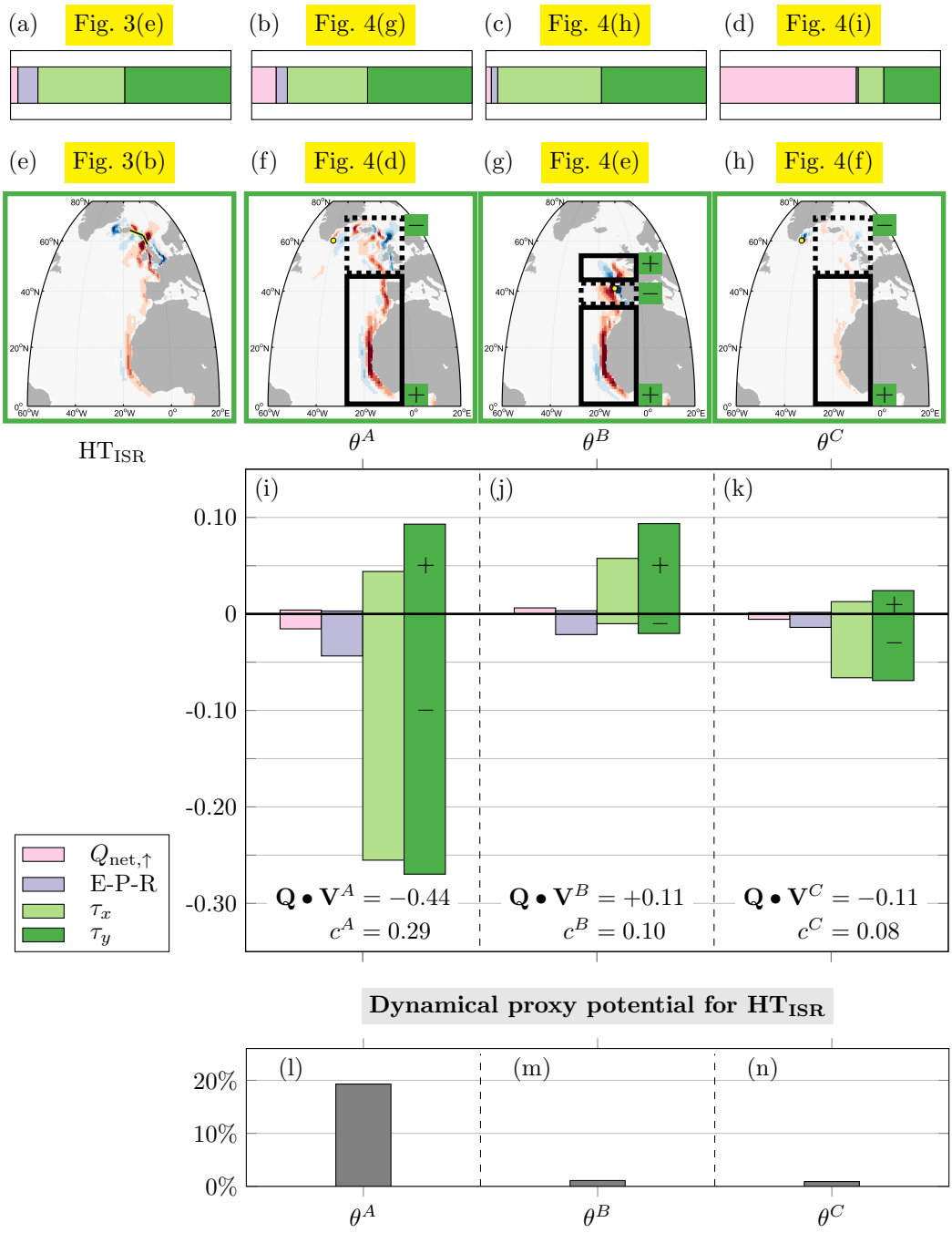

Figure 7. (a)-(h): Replots of subpanels in Figs. 3 and 4, as indicated by the yellow labels. (i)-(k): Contributions from the forcings $F = Q_{\mathrm{net},\uparrow}, \text{E-P-R}, \tau_x, \tau_y$ to the projection $\mathbf{Q} \bullet \mathbf{V}^\star$ (eq. (11)), where (i) $\star = A$, (j) $\star = B$, and (k) $\star = C$. The projections are computed as shown in Fig. 6. That is, in each of the subpanels (i)-(k), the τ_y-contribution is computed by projecting the sensitivity map $\sigma_{\mathrm{HT}}^{-1} \frac{\partial(\mathrm{HT}_{\mathrm{ISR}})}{\partial \tau_y} \Delta\tau_y$ (shown in (e)) onto the respective sensitivity map $\sigma_\star^{-1} \frac{\partial \theta^\star}{\partial \tau_y} \Delta\tau_y$ (shown in (f) for $\star = A$, (g) for $\star = B$, (h) for $\star = C$). Positive (negative) τ_y-contributions, arise in the Atlantic subregion inside the black solid (dashed) box in (f) for $\star = A$, (g) for $\star = B$, (h) for $\star = C$, inside which sensitivities correlate (anticorrelate) with those in subpanel (e). The value for $\mathbf{Q} \bullet \mathbf{V}^\star$ (bottom of subpanels (i)-(k)) is obtained by summing up all upward- and downward pointing bars in the respective subpanel. Here, destructive interference is quantified by $c^\star$ (eq. (12)). (l)-(n): Dynamical proxy potential of (l) θ^A, (m) θ^B, (n) θ^C for $\mathrm{HT}_{\mathrm{ISR}}$, computed by squaring $\mathbf{Q} \bullet \mathbf{V}^\star$ obtained in (i),(j),(k), respectively (cf. eq. (5)).

adjustment physics or (ii) uncertainty quantification (cf. Fig. 1(c)). As for (i), $\mathrm{HT_{ISR}}$ shares 19% of its dynamical causes and controls with θ^A, but only 1% with θ^B and θ^C. As a result, θ^A (θ^B, θ^C) captures 19% (1%, 1%) of the variability of $\mathrm{HT_{ISR}}$, taking into account all potential forcing scenarios. As for (ii), dynamical proxy potential predicts that uncertainty in $\mathrm{HT_{ISR}}$ would get reduced by 19% (1%, 1%), if a noise-free measurement value of θ^A (θ^B, θ^C) was added to the state estimation framework that was described in section 3.1.

4 Summary and Discussion

The design of effective climate observing systems relies on a both *physical* and *quantitative* understanding of which processes are captured by existing and future observations and which quantities of interests (QoIs) that capture important aspects of the climate system can be informed. Toward this goal, we introduced the concept of dynamical proxy potential - a tool for ocean observing system design which is rooted in both (i) dynamical and (ii) quantitative principles. To establish this tool, our approach was to expose the potential of optimal observing system design, an emerging branch of computational science and engineering, in the context of ocean state estimation for climate. We applied the general theoretical framework (as laid out, e.g., in Flath et al. (2011); Bui-Thanh et al. (2012, 2013); Isaac et al. (2015)) to the ECCO version 4 estimation framework, and, importantly, provided ocean dynamical interpretations. For pedagogical reasons, this paper simplifies the general framework in three important ways: (1) only one observational asset is considered, (2) observations are treated as noise-free, and (3) the QoI, observations and uncertain control variables are defined as five-year mean quantities. We note, however, that the concept is readily generalized to cases where all of the restrictions are relaxed, and we will present such generalized applications in forthcoming work. In the following, we summarize the results from our exemplifying case study, point out potential limitations, and provide specific directions for future work.

In this work, heat transport across the Iceland-Scotland ridge ($\mathrm{HT_{ISR}}$) was the exemplary QoI. We explored the potential for three example observed quantities to serve as proxies for this QoI: two temperature observations, θ^A, θ^C, in the Irminger Sea, and one temperature observation, θ^B, off the Portuguese coast. Here, θ^A, θ^B were assumed subsurface, and θ^C at the sea surface. Examination of the sensitivity matrices of the QoI and observations - exposing all viable adjustment processes - revealed the following. On a five-year time scale, $\mathrm{HT_{ISR}}$ and θ^A are most sensitive to changes in wind forcing in two main regions: (I) along the eastern boundary of the Atlantic and (II) in the northeast Atlantic and the Nordic Seas. Wind forcing in region (I) excites a pressure adjustment mechanism, which strengthens (or weakens) both the ISR geostrophic transport and the Irminger Current, leading to anomalies in $\mathrm{HT_{ISR}}$ and θ^A of equal sign. Wind forcing in region (II) drives a barotropic circulation around Iceland which simultaneously strengthens (or weakens) the Norwegian Atlantic and East Greenland Currents, leading to anomalies in θ^A and $\mathrm{HT_{ISR}}$ of opposite sign.

Dynamical proxy potential is computed by projecting the sensitivity matrices of the QoI and observation under consideration, by way of eq. (5). This projection effectively superimposes all viable sensitivity pathways and measures the degree of shared adjustment physics, taking into account the effects of constructive and destructive interference of information propagation. Destructive interference of information occurs because wind forcing in region (I) leads to responses in $\mathrm{HT_{ISR}}$ and θ^A of equal sign, while wind forcing in region (II) leads to responses in $\mathrm{HT_{ISR}}$ and θ^A of opposite sign. Considering the five-year mean of the two quantities, we find that the dynamical proxy potential of θ^A for $\mathrm{HT_{ISR}}$ is 19%. Dynamical proxy potential allows two equivalent interpretations: θ^A (i) shares 19% of its adjustment physics with $\mathrm{HT_{ISR}}$; (ii) reduces the uncertainty in $\mathrm{HT_{ISR}}$ by 19%, if θ^A is added as noise-free to the ECCO state estimate.

The example presented in this work highlights four important results, which generalize beyond the case study.

(1) Conventionally, hydrographic observations are used for inferring two types of information: first, local ocean temperature and salinity; and second, the geostrophic transport across an oceanic section, if hydrographic profiles at the end points of the section (and thus, along-section density gradients) are available. Based on endpoint geostrophy, moorings that are to be informative for cross-ISR transport would be located along the ISR itself. Here, we demonstrated that *remote hydrographic observations can provide strong constraints* on cross-section transports due to large-scale oceanic teleconnections. This result highlights the importance of further probing dynamical constraints contained within the existing observational database.

(2) The information that the observation θ^A provides for the QoI $\mathrm{HT}_{\mathrm{ISR}}$ originates in the observation's potential to capture a certain degree of the variability of $\mathrm{HT}_{\mathrm{ISR}}$ - a similar concept that underlies statistical proxy potential. However, in contrast to statistical proxy potential, dynamical proxy potential only accounts for covariability that has a dynamical underpinning, by employing sensitivity information that traces variability of $\mathrm{HT}_{\mathrm{ISR}}$ and θ^A back to its origins in local or remote forcing. The dominant regions, (I),(II), and associated shared wind-driven adjustment mechanisms discussed in this study, have been shown to be key for many distinct oceanic quantities (see adjoint-based investigations referenced in the introduction) and reflect the ubiquitous nature of basin-scale barotropic and baroclinic adjustment processes (D. P. Marshall & Johnson, 2013, and references therein). Uncovering basin-scale teleconnections and *common dynamical pathways and mechanisms* via which many oceanic QoIs adjust, as performed here, may help to (i) explain the physical cause of observed variability in the North Atlantic, and (ii) build efficient observing systems which capture these mechanisms reliably.

(3) In contrast to statistical proxy potential, dynamical proxy potential does not provide a direct recipe for recovering the QoI (here: $\mathrm{HT}_{\mathrm{ISR}}$), from existing measurements (here: of θ^A). Instead, the framework of ocean state estimation is required to extract the measurements' constraint exerted on the QoI. An important fact - with *implications for observing system design* - is that, independent of the measurement value, potentially taken by a *future* observing system, inclusion of the observation will reduce uncertainty in the QoI by the pre-determined dynamical proxy potential (here: 19%, assuming a noise-free observation). While ocean state estimation is a well-established method for optimally combining ocean observations with an ocean general circulation model (Heimbach et al., 2019), the way in which observations constrain QoIs (other than the actual model-data misfit function to be minimized) in the ocean state estimate have remained unexplored. The computational framework for quantifying dynamical proxy potential, as introduced in this work, provides the first clear and dynamical interpretation of UQ and observational constraints in ocean state estimation.

(4) In our case study, destructive interference of competing adjustment mechanisms in regions (I) and (II) prevents the dynamical proxy potential of θ^A for $\mathrm{HT}_{\mathrm{ISR}}$ from exceeding 19%. The method introduced in this work *quantifies missing information and constructive & destructive interference*, paving the way for extracting complementary information from further observations. In our case study, we found that θ^B is sensitive to wind forcing in region (I), but entirely insensitive to wind forcing in region (II). A forthcoming paper will show that considering θ^A and θ^B in combination, will help to extract some of the information which is lost in destructive interference when viewing θ^A in isolation.

The adjoint of an ocean general circulation model is the key tool for obtaining complete sensitivity information to local and remote forcing. This sensitivity information, in turn, is the cornerstone of the quantification of dynamical proxy potential, laying the groundwork for dynamics-based observing system design. In previous work, adjoint-derived sensitivity information has been proposed to support observing system design in a distinct fashion: Marotzke et al. (1999), Heimbach et al. (2011), and Köhl and Stammer (2004) use an adjoint model to compute sensitivities of a given QoI to hydrographic state variables or hydrographic observations, and suggest that regions of highest sensitivity are to be prioritized when deploying new hydrographic observations. Following this recipe and choosing heat transport across the Greenland-Scotland ridge (GSR) as their QoI, Köhl and Stammer (2004) find highest sensitivity (or 'optimal' hydrographic observations) close to the GSR itself, consistent with the dynamical principle of endpoint geostrophy (see discussion point (1) above). In this fashion, the philosophy of previous adjoint-based studies is to discover direct cause and effect relationships between changes in observations and changes in the QoI. Dynamical proxy potential, as introduced in this work, looks further: by employing sensitivity information of not only the QoI, but also of the observations, dynamical proxy potential quantifies dynamics-based covariability of the QoI and observations, driven by local or remote forcings. As a result, dynamical proxy potential can exploit that multiple distinct QoIs may be connected by basin-wide dynamical adjustments and thus well constrained by limited instrumentation in this shared adjustment pathway. Moreover, unlike dynamical proxy potential, the previous adjoint-based method do not provide a *quantitative* estimate on how much information the suggested observations contain on the QoI (and how much information is missing). Instead, the previous method provides only a relative estimate by suggesting that some observations may be more informative than others.

In the context of Arctic observing system design, Kaminski et al. (2015, 2018) utilized a method related to the one presented in this work. A key difference is that the authors handle sensitivity information averaged over large regions (e.g., Fig. 2 in Kaminski et al., 2015). While spatially averaged sensitivity enables numerically efficient quantification of the constraint from large-scale data acquisitions (e.g., from satellite or aircraft), it could entail large aggregation errors (Kaminski et al., 2001). Furthermore, we argue that it inhibits clear understanding of proxy origins, by grouping information from dynamically distinct regions. This is especially true for harnessing proxy potential from shared wind-driven adjustments, for which resolution of the coastal waveguides is key.

While the adjoint model provides comprehensive sensitivity information throughout the global model domain, adjoint-derived sensitivity is limited by the linear approximation and inexactness of the adjoint (Czeschel et al., 2010; Errico, 1997; Hoteit et al., 2005; Forget et al., 2015). Perturbation experiments with the full nonlinear model dynamics in Appendix A show that the adjoint-derived sensitivities in our case study reliably capture the basin-wide adjustment mechanism that are excited by wind stress perturbations in regions (I) and (II). However, estimation errors in the predicted response amplitudes can reach up to 20% - partly due to the linear approximation, and partly due to the inexactness of the adjoint. This emphasizes that we must keep validating the accuracy of adjoint-derived sensitivity information and that improving the exactness of the adjoint would add great value to dynamics-based observing system design.

A second shortcoming of the methodology presented here is that dynamical proxy potential may be dependent on the underlying ocean GCM. Global ocean GCMs are typically too coarse (here: of $1\,^\circ$ horizontal resolution) to accurately represent density-driven gravity currents (e.g., across overflow regions in the subpolar North Atlantic), deep convection, and narrow boundary currents. Inability to test model dependency, due to unavailable adjoints for almost all GCMs, is a limiting factor.

As a third drawback, important limiting assumptions entering the calculation of dynamical proxy potential are the choice of forcing variables and the associated weights.

The forcing variables should include all uncertain elements in the model, i.e., the parts that are not determined by the known governing equations. In ocean state estimation, the uncertain variables are assumed to consist of atmospheric forcing variables, initial conditions, and parameters that are used for empirical, constitutive laws (such as mixing of tracers and momentum) and subgrid-scale parameterization (Forget et al., 2015), while structural model uncertainties or model inadequacy remain unrepresented. The associated weights reflect prior uncertainties in the forcing variables. In the choice of uncertain variables and weights, the notion of dynamical proxy potential follows the assumptions of ocean state estimation. It is important to note that, while the sensitivity matrices uncover all dynamical processes (independent of the weights), the relative importance of these mechanisms is determined by the weights.

In our case study, we investigated how changes in time-mean forcing affects the time-means of temperature observations (e.g., θ^A) and QoI ($\mathrm{HT}_{\mathrm{ISR}}$), on five-year time scales. Thereby, we identified key forcings, adjustment pathways, and mechanisms for observations and QoI, but did not disentangle whether the dominating mechanisms operate on weekly, monthly, seasonal, annual, or multiannual ($<$ five years) time scales. Future work should consider time-variable changes in forcing and investigate the variability of observations and QoIs on shorter (e.g., interannual) time scales. This will enable us to not only disentangle the dominant time scales of the operating mechanisms, but also to assess the predictive skill of observations for a QoI, if the QoI's response to certain forcings is lagged behind the observations' response. In view of the recently deployed OSNAP mooring array, it will be exciting to explore the dynamical proxy potential of the OSNAP observations for remote oceanic quantities that are not readily accessible to direct observation but have important climatic repercussions.

A further future direction is to extend the notion of dynamical proxy potential by taking into account observational noise as well as data redundancy and complementarity between multiple observations - an effort to be pursued in a forthcoming paper. By targeting information that is complementary to existing observing systems, the notion of dynamical proxy potential can support the design of effective future observing systems. An interesting question is that of an optimal observing strategy, for instance: what is the value of surface (possibly remotely sensed) vs. subsurface (in situ) observations for unobserved or unobservable QoIs? In our case study, we found that the surface temperature observation θ^C is too sensitive to local air-sea heat exchanges. The strong sensitivity to local processes overrides the sensitivity to the large-scale basin-wide adjustment mechanisms that are relevant for $\mathrm{HT}_{\mathrm{ISR}}$ - and potentially many other QoIs. The fact that the efficiency of observing systems depends on the targeted QoIs highlights the importance of an ongoing community discussion on which climate QoIs are most important to constrain.

The oceanographic community needs a synergistic, quantitative approach to codesign a cost-effective, long-term, and sustained observing system of the North Atlantic. In this work, we have introduced a dynamics-based alternative to statistical correlations and conventional observing system simulation experiments (OSSEs). With a focus on understanding and exploiting the underlying dynamics of covariability, we hope that our new approach can contribute to maximizing the information from existing and future observing systems.

Appendix A Linear Approximation and Inexactness of the Adjoint

The adjoint of an ocean GCM provides sensitivity information (eqs. (1),(2)) which is the key ingredient of dynamical proxy potential. Caveats are that (i) the sensitivity information is only a linear approximation for the nonlinear responses in QoIs and observations to perturbations, and that (ii) the adjoint may be inexact, e.g., due to artifically increased viscosity compared to the foward model, which is often a requirement

to stabilize the adjoint (Hoteit et al., 2005, 2010; Forget et al., 2015). Here, we verify the adjoint-derived sensitivities against forward perturbation experiments with the nonlinear forward model. Our control simulation covers the final five years of the ECCOv4r2 state estimate. We focus on meridional wind stress perturbations inside the two green regions in Fig. 5, along the western African coast and the western Icelandic coast.

For each of the two chosen regions, we perform two separate perturbation experiments, imposing meridional wind stress anomalies of $\Delta\tau_y = \pm 0.05\,\mathrm{N/m^2}$ inside the region, respectively. We maintain the wind stress perturbation over the full five-year period. For $J \in \{\theta^A, \theta^B, \mathrm{HT_{ISR}}\}$ (eqs. (6),(7)), we then compute the differences

$$\Delta^{\pm}_{\mathrm{fwd}} J := J^{\pm} - J^0.$$

Here, J^0 denotes the quantity J in the control simulation, and J^+ and J^- the same quantity in the simulation with the positive and negative perturbation, respectively. $\Delta^+_{\mathrm{fwd}} J$ and $-\Delta^-_{\mathrm{fwd}} J$ are identical if J depends linearly on τ_y inside the chosen perturbation region. Even if a resemblance of $\Delta^+_{\mathrm{fwd}} J$ and $-\Delta^-_{\mathrm{fwd}} J$ suggests a linear response, the adjoint-derived anomalies can still deviate from the forward anomalies, due to inexactness of the adjoint. Therefore, we next compare the forward anomalies $\Delta^+_{\mathrm{fwd}} J$ and $-\Delta^-_{\mathrm{fwd}} J$ to the adjoint estimate

$$\Delta^+_{\mathrm{adj}} J := \frac{\partial J}{\partial \tau_y} \cdot \Delta\tau_y,$$

where $\Delta\tau_y$ now denotes the positive meridional wind stress anomaly ($+0.05\,\mathrm{N/m^2}$ inside the chosen region).

Fig. A1 shows the comparison of the time-mean anomalies $\Delta^+_{\mathrm{fwd}} J$ (solid horizontal lines), $-\Delta^-_{\mathrm{fwd}} J$ (dashed horizontal lines), and $\Delta^+_{\mathrm{adj}} J$ (horizontal lines with triangles), in response to wind stress anomalies along the western African coast (Figs. A1(a),(b)) and along the western Icelandic coast (Figs. A1(c),(d)). Figs. A1(a),(c) show response anomalies in $J = \theta^A, \theta^B$ (while in Fig. A1(c), the response in $J = \theta^B$ is invisible, being two orders of magnitude smaller than the response in $J = \theta^A$), and Figs. A1(b),(d) response anomalies in $J = \mathrm{HT_{ISR}}$. Note that the solid horizontal lines in Figs. A1(a),(c) correspond to the time-mean temperature anomalies at 300 m depth, found at the yellow dots in Figs. 5(a),(b), respectively. In Figs. A1(a)-(d), the solid and dashed thin lines show the time-evolving response anomalies in J from the forward perturbation experiments (as a function of years since the start of the perturbation), which the solid and dashed horizontal lines ($\Delta^+_{\mathrm{fwd}} J$ and $-\Delta^-_{\mathrm{fwd}} J$) are the time-average of.

In Fig. A1, we see notable deviations between $\Delta^+_{\mathrm{fwd}} J$ and $-\Delta^-_{\mathrm{fwd}} J$ in two cases: for the anomalies in $J = \theta^B$ in response to a wind stress perturbation along the western African coast (green solid vs. dashed horizontal lines in Fig. A1(a)), and for the anomaly in $J = \theta^A$ in response to a wind stress perturbation along the western Icelandic coast (orange solid vs. dashed horizontal lines in Fig. A1(c)). In both cases, the amplitudes of the time-evolving forward anomalies start to develop an offset after 1-2 years. Since anomalies in θ^A and θ^B are the time-integrated result of ocean transport anomalies, the offset tends to becomes larger over time. In contrast, $\Delta^+_{\mathrm{fwd}} \mathrm{HT_{ISR}}$ and $-\Delta^-_{\mathrm{fwd}} \mathrm{HT_{ISR}}$ coincide (purple solid vs. dashed horizontal lines in Fig. A1(b),(d)), suggesting that $\mathrm{HT_{ISR}}$ is linear as a function of τ_y forcing in the tested perturbation regions. Note however that, despite the suggested linearity, $\Delta^+_{\mathrm{adj}} \mathrm{HT_{ISR}}$ slightly differs from the forward anomalies in Fig. A1(d) (purple horizontal lines with vs. without triangles), due to an inexact adjoint. A similar situation occurs in Fig. A1(a) for the response anomalies in θ^A (orange horizontal lines with vs. without triangles). In all cases shown in Fig. A1, the adjoint estimate $\Delta^+_{\mathrm{adj}} J$ predicts the response anomalies in J with the correct sign. Moreover, predicted amplitudes are generally close to those of the forward anomalies, although, in few cases, they can be off by up to 20%.

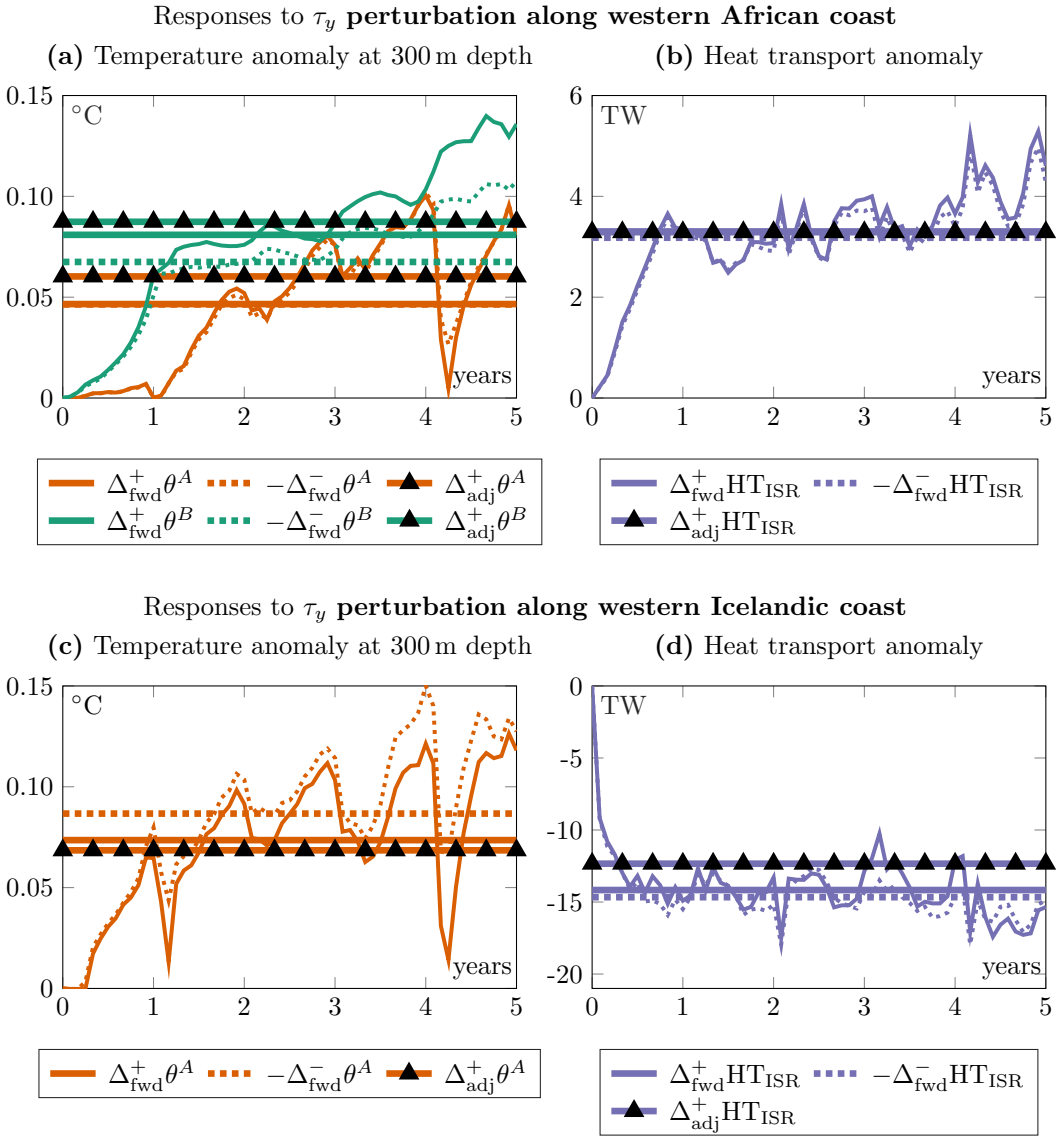

Figure A1. Anomalies in (a),(c) $J = \theta^A, \theta^B$, and (b),(d) $J = \text{HT}_{\text{ISR}}$, in response to meridional wind stress (τ_y) perturbations along the (a),(b) western African coast and (c),(d) western Icelandic coast. The solid and dashed horizontal lines show the anomalies $\Delta^+_{\text{fwd}}J$ and $-\Delta^-_{\text{fwd}}J$ from the nonlinear forward perturbation experiments (computed as the five-year mean of the thin solid and dashed time-evolving lines, respectively). The horizontal lines with triangles show the adjoint-derived anomalies $\Delta^+_{\text{adj}}J$.

Acknowledgments

N.L. and K.H.N. were supported by the ice2ice project funded by the European Research Council under the European Community Seventh Framework Programme (FP7/2007-2013)/ERC Grant Agreement 610055. P.H. and H.R.P. received funding in part from NSF OCE grant #1924456 and the Estimating the Circulation and Climate of the Ocean (ECCO) project via a JPL/Caltech subcontract. The ECCOv4r2 model setup used in this work is available for download on Github (https://github.com/gaelforget/ECCOv4) as an instance of the MIT general circulation model (MITgcm, http://mitgcm.org/). Adjoint code was generated using the TAF software tool, created and maintained by FastOpt GmbH (http://www.fastopt.com/). We wish to thank Céline Heuzé, Andrew Moore, Tim Smith, Carl Wunsch, and Daniel Jones for helpful discussions.

References

Alexanderian, A., Petra, N., Stadler, G., & Ghattas, O. (2016). A Fast and Scalable Method for A-Optimal Design of Experiments for Infinite-dimensional Bayesian Nonlinear Inverse Problems. *SIAM Journal on Scientific Computing*, *38*(1), A243–A272. doi: 10.1137/140992564

Alexander-Turner, R., Ortega, P., & Robson, J. I. (2018). How Robust Are the Surface Temperature Fingerprints of the Atlantic Overturning Meridional Circulation on Monthly Time Scales? *Geophysical Research Letters*, *45*(8), 3559–3567. doi: 10.1029/2017GL076759

Årthun, M., & Eldevik, T. (2016). On Anomalous Ocean Heat Transport toward the Arctic and Associated Climate Predictability. *Journal of Climate*, *29*(2), 689–704. doi: 10.1175/JCLI-D-15-0448.1

Asbjørnsen, H., Årthun, M., Skagseth, Ø., & Eldevik, T. (2019). Mechanisms of Ocean Heat Anomalies in the Norwegian Sea. *Journal of Geophysical Research: Oceans*, *124*(4), 2908–2923. doi: 10.1029/2018JC014649

Baehr, J., Haak, H., Alderson, S., Cunningham, S. A., Jungclaus, J. H., & Marotzke, J. (2007). Timely Detection of Changes in the Meridional Overturning Circulation at 26°N in the Atlantic. *Journal of Climate*, *20*(23), 5827–5841. doi: 10.1175/2007JCLI1686.1

Berx, B., Hansen, B., Østerhus, S., Larsen, K. M., Sherwin, T., & Jochumsen, K. (2013). Combining in situ measurements and altimetry to estimate volume, heat and salt transport variability through the Faroe-Shetland Channel. *Ocean Science*, *9*(4), 639–654. doi: 10.5194/os-9-639-2013

Bingham, R. J., & Hughes, C. W. (2009). Signature of the Atlantic meridional overturning circulation in sea level along the east coast of North America. *Geophysical Research Letters*, *36*(2). doi: 10.1029/2008GL036215

Buckley, M. W., Ponte, R. M., Forget, G., & Heimbach, P. (2014). Low-Frequency SST and Upper-Ocean Heat Content Variability in the North Atlantic. *Journal of Climate*, *27*(13), 4996–5018. doi: 10.1175/JCLI-D-13-00316.1

Bui-Thanh, T., Burstedde, C., Ghattas, O., Martin, J., Stadler, G., & Wilcox, L. C. (2012). Extreme-scale UQ for Bayesian Inverse Problems Governed by PDEs. In *Proceedings of the International Conference on High Performance Computing, Networking, Storage and Analysis* (pp. 1–11).

Bui-Thanh, T., Ghattas, O., Martin, J., & Stadler, G. (2013). A Computational Framework for Infinite-Dimensional Bayesian Inverse Problems Part I: The Linearized Case, with Application to Global Seismic Inversion. *SIAM Journal on Scientific Computing*, *35*(6), A2494–A2523. doi: 10.1137/12089586X

Caesar, L., Rahmstorf, S., Robinson, A., Feulner, G., & Saba, V. (2018). Observed fingerprint of a weakening Atlantic Ocean overturning circulation. *Nature*, *556*(7700), 191–196. doi: 10.1038/s41586-018-0006-5

Czeschel, L., Eden, C., & Greatbatch, R. J. (2012). On the Driving Mechanism of the Annual Cycle of the Florida Current Transport. *Journal of Physical*

Oceanography, *42*(5), 824–839. doi: 10.1175/JPO-D-11-0109.1

Czeschel, L., Marshall, D. P., & Johnson, H. L. (2010). Oscillatory sensitivity of Atlantic overturning to high-latitude forcing. *Geophysical Research Letters*, *37*(10), L10601. doi: 10.1029/2010GL043177

Errico, R. M. (1997). What Is an Adjoint Model? *Bulletin of the American Meteorological Society*, *78*(11), 2577–2591. doi: 10.1175/1520-0477(1997)078⟨2577:WIAAM⟩2.0.CO;2

Ezer, T. (2015). Detecting changes in the transport of the Gulf Stream and the Atlantic overturning circulation from coastal sea level data: The extreme decline in 2009-2010 and estimated variations for 1935-2012. *Global and Planetary Change*, *129*, 23–36. doi: 10.1016/j.gloplacha.2015.03.002

Flath, H., Wilcox, L., Akçelik, V., Hill, J., van Bloemen Waanders, B., & Ghattas, O. (2011). Fast Algorithms for Bayesian Uncertainty Quantification in Large-Scale Linear Inverse Problems Based on Low-Rank Partial Hessian Approximations. *SIAM Journal on Scientific Computing*, *33*(1), 407–432. doi: 10.1137/090780717

Forget, G., Campin, J.-M., Heimbach, P., Hill, C. N., Ponte, R. M., & Wunsch, C. (2015). ECCO version 4: an integrated framework for non-linear inverse modeling and global ocean state estimation. *Geosci. Model Dev.*, *8*(10), 3071–3104. doi: 10.5194/gmd-8-3071-2015

Frajka-Williams, E. (2015). Estimating the Atlantic overturning at 26°N using satellite altimetry and cable measurements. *Geophysical Research Letters*, *42*(9), 3458–3464. doi: 10.1002/2015GL063220

Frajka-Williams, E., Ansorge, I. J., Baehr, J., Bryden, H. L., Chidichimo, M. P., Cunningham, S. A., ... Wilson, C. (2019). Atlantic Meridional Overturning Circulation: Observed Transport and Variability. *Frontiers in Marine Science*, *6*. doi: 10.3389/fmars.2019.00260

Fukumori, I., Wang, O., Llovel, W., Fenty, I., & Forget, G. (2015). A near-uniform fluctuation of ocean bottom pressure and sea level across the deep ocean basins of the Arctic Ocean and the Nordic Seas. *Progress in Oceanography*, *134*, 152–172. doi: 10.1016/j.pocean.2015.01.013

Galanti, E., & Tziperman, E. (2003). A Midlatitude-ENSO Teleconnection Mechanism via Baroclinically Unstable Long Rossby Waves. *Journal of Physical Oceanography*, *33*(9), 1877–1888. doi: 10.1175/1520-0485(2003)033⟨1877:AMTMVB⟩2.0.CO;2

Galanti, E., Tziperman, E., Harrison, M., Rosati, A., Giering, R., & Sirkes, Z. (2002). The Equatorial Thermocline Outcropping–A Seasonal Control on the Tropical Pacific Ocean-Atmosphere Instability Strength. *Journal of Climate*, *15*(19), 2721–2739. doi: 10.1175/1520-0442(2002)015⟨2721:TETOAS⟩2.0.CO;2

Giering, R., & Kaminski, T. (1998). Recipes for Adjoint Code Construction. *ACM Trans. Math. Softw.*, *24*(4), 437–474. doi: 10.1145/293686.293695

Hansen, B., Larsen, K. M. H., Hátún, H., Kristiansen, R., & Mortensen, S., E. a Østerhus. (2015). Transport of volume, heat, and salt towards the Arctic in the Faroe Current 1993-2013. *Ocean Science*, *11*(5), 743–757. doi: 10.5194/os-11-743-2015

Hansen, B., & Østerhus, S. (2000). North Atlantic–Nordic Seas exchanges. *Progress in Oceanography*, *45*(2), 109–208. doi: 10.1016/S0079-6611(99)00052-X

Hansen, B., Østerhus, S., Hátún, H., Kristiansen, R., & Larsen, K. M. H. (2003). The Iceland-Faroe inflow of Atlantic water to the Nordic Seas. *Progress in Oceanography*, *59*(4), 443–474. doi: 10.1016/j.pocean.2003.10.003

Heimbach, P., Fukumori, I., Hill, C. N., Ponte, R. M., Stammer, D., Wunsch, C., ... Zhang, H. (2019). Putting It All Together: Adding Value to the Global Ocean and Climate Observing Systems With Complete Self-Consistent Ocean State and Parameter Estimates. *Frontiers in Marine Science*, *6*. doi:

10.3389/fmars.2019.00055

Heimbach, P., Wunsch, C., Ponte, R. M., Forget, G., Hill, C., & Utke, J. (2011). Timescales and regions of the sensitivity of Atlantic meridional volume and heat transport: Toward observing system design. *Deep Sea Research Part II: Topical Studies in Oceanography*, *58*(17-18), 1858–1879. doi: 10.1016/j.dsr2.2010.10.065

Hoteit, I., Cornuelle, B., & Heimbach, P. (2010). An eddy-permitting, dynamically consistent adjoint-based assimilation system for the tropical Pacific: Hindcast experiments in 2000. *Journal of Geophysical Research: Oceans*, *115*(C3), C03001. doi: 10.1029/2009JC005437

Hoteit, I., Cornuelle, B., Köhl, A., & Stammer, D. (2005). Treating strong adjoint sensitivities in tropical eddy-permitting variational data assimilation. *Quarterly Journal of the Royal Meteorological Society*, *131*(613), 3659–3682. doi: 10.1256/qj.05.97

Isaac, T., Petra, N., Stadler, G., & Ghattas, O. (2015). Scalable and efficient algorithms for the propagation of uncertainty from data through inference to prediction for large-scale problems, with application to flow of the Antarctic ice sheet. *Journal of Computational Physics*, *296*, 348–368. doi: 10.1016/j.jcp.2015.04.047

Jones, D., Forget, G., Sinha, B., Josey, S., Boland, E., Meijers, A., & Shuckburgh, E. (2018). Local and Remote Influences on the Heat Content of the Labrador Sea: An Adjoint Sensitivity Study. *Journal of Geophysical Research: Oceans*, *0*(0). doi: 10.1002/2018JC013774

Kaminski, T., Kauker, F., Eicken, H., & Karcher, M. (2015). Exploring the utility of quantitative network design in evaluating Arctic sea ice thickness sampling strategies. *The Cryosphere*, *9*(4), 1721–1733. doi: 10.5194/tc-9-1721-2015

Kaminski, T., Kauker, F., Toudal Pedersen, L., Voßbeck, M., Haak, H., Niederdrenk, L., ... Gråbak, O. (2018). Arctic Mission Benefit Analysis: impact of sea ice thickness, freeboard, and snow depth products on sea ice forecast performance. *The Cryosphere*, *12*(8), 2569–2594. doi: https://doi.org/10.5194/tc-12-2569-2018

Kaminski, T., Rayner, P. J., Heimann, M., & Enting, I. G. (2001). On aggregation errors in atmospheric transport inversions. *Journal of Geophysical Research: Atmospheres*, *106*(D5), 4703–4715. doi: 10.1029/2000JD900581

Knight, J. R., Allan, R. J., Folland, C. K., Vellinga, M., & Mann, M. E. (2005). A signature of persistent natural thermohaline circulation cycles in observed climate. *Geophysical Research Letters*, *32*(20). doi: 10.1029/2005GL024233

Köhl, A. (2005). Anomalies of Meridional Overturning: Mechanisms in the North Atlantic. *Journal of Physical Oceanography*, *35*(8), 1455–1472. doi: 10.1175/JPO2767.1

Köhl, A., & Stammer, D. (2004). Optimal Observations for Variational Data Assimilation. *Journal of Physical Oceanography*, *34*(3), 529–542. doi: 10.1175/2513.1

Landerer, F. W., Wiese, D. N., Bentel, K., Boening, C., & Watkins, M. M. (2015). North Atlantic meridional overturning circulation variations from GRACE ocean bottom pressure anomalies. *Geophysical Research Letters*, *42*(19), 8114–8121. doi: 10.1002/2015GL065730

Latif, M., Roeckner, E., Botzet, M., Esch, M., Haak, H., Hagemann, S., ... Mitchell, J. (2004). Reconstructing, Monitoring, and Predicting Multidecadal-Scale Changes in the North Atlantic Thermohaline Circulation with Sea Surface Temperature. *Journal of Climate*, *17*(7), 1605–1614. doi: 10.1175/1520-0442(2004)017⟨1605:RMAPMC⟩2.0.CO;2

Lherminier, P., Mercier, H., Gourcuff, C., Alvarez, M., Bacon, S., & Kermabon, C. (2007). Transports across the 2002 Greenland-Portugal Ovide section and comparison with 1997. *Journal of Geophysical Research: Oceans*, *112*(C7). doi:

10.1029/2006JC003716

Little, C. M., Hu, A., Hughes, C. W., McCarthy, G. D., Piecuch, C. G., Ponte, R. M., & Thomas, M. D. (2019). The Relationship Between U.S. East Coast Sea Level and the Atlantic Meridional Overturning Circulation: A Review. *Journal of Geophysical Research: Oceans*, *124*(9), 6435–6458. doi: 10.1029/2019JC015152

Lopez, H., Goni, G., & Dong, S. (2017). A reconstructed South Atlantic Meridional Overturning Circulation time series since 1870. *Geophysical Research Letters*, *44*(7), 3309–3318. doi: 10.1002/2017GL073227

Lozier, M. S., Bacon, S., Bower, A. S., Cunningham, S. A., Femke de Jong, M., de Steur, L., ... Zika, J. D. (2017). Overturning in the Subpolar North Atlantic Program: A New International Ocean Observing System. *Bulletin of the American Meteorological Society*, *98*(4), 737–752. doi: 10.1175/BAMS-D-16-0057.1

Lozier, M. S., Li, F., Bacon, S., Bahr, F., Bower, A. S., Cunningham, S. A., ... Zhao, J. (2019). A sea change in our view of overturning in the subpolar North Atlantic. *Science*, *363*(6426), 516–521. doi: 10.1126/science.aau6592

Marotzke, J., Giering, R., Zhang, K. Q., Stammer, D., Hill, C., & Lee, T. (1999). Construction of the adjoint MIT ocean general circulation model and application to Atlantic heat transport sensitivity. *Journal of Geophysical Research: Oceans*, *104*(C12), 29529–29547. doi: 10.1029/1999JC900236

Marshall, D. P., & Johnson, H. L. (2013). Propagation of Meridional Circulation Anomalies along Western and Eastern Boundaries. *Journal of Physical Oceanography*, *43*(12), 2699–2717. doi: 10.1175/JPO-D-13-0134.1

Marshall, J., Adcroft, A., Hill, C., Perelman, L., & Heisey, C. (1997). A finite-volume, incompressible Navier Stokes model for studies of the ocean on parallel computers. *Journal of Geophysical Research: Oceans*, *102*(C3), 5753–5766. doi: 10.1029/96JC02775

Marshall, J., Hill, C., Perelman, L., & Adcroft, A. (1997). Hydrostatic, quasi-hydrostatic, and nonhydrostatic ocean modeling. *Journal of Geophysical Research: Oceans*, *102*(C3), 5733–5752. doi: 10.1029/96JC02776

McCarthy, G. D., Brown, P. J., Flagg, C. N., Goni, G., Houpert, L., Hughes, C. W., ... Smeed, D. A. (2019). Sustainable observations of the AMOC: Methodology and Technology. *Reviews of Geophysics*, *58*(1), e2019RG000654. doi: 10.1029/2019RG000654

McCarthy, G. D., Haigh, I. D., Hirschi, J. J.-M., Grist, J. P., & Smeed, D. A. (2015). Ocean impact on decadal Atlantic climate variability revealed by sea-level observations. *Nature*, *521*(7553), 508–510. doi: 10.1038/nature14491

Mercier, H., Lherminier, P., Sarafanov, A., Gaillard, F., Daniault, N., Desbruyères, D., ... Thierry, V. (2015). Variability of the meridional overturning circulation at the Greenland-Portugal OVIDE section from 1993 to 2010. *Progress in Oceanography*, *132*, 250–261. doi: 10.1016/j.pocean.2013.11.001

Orvik, K. A., & Skagseth, Ø. (2005). Heat flux variations in the eastern Norwegian Atlantic Current toward the Arctic from moored instruments, 1995-2005. *Geophysical Research Letters*, *32*(14). doi: 10.1029/2005GL023487

Østerhus, S., Turrell, W. R., Jónsson, S., & Hansen, B. (2005). Measured volume, heat, and salt fluxes from the Atlantic to the Arctic Mediterranean. *Geophysical Research Letters*, *32*(7). doi: 10.1029/2004GL022188

Østerhus, S., Woodgate, R., Valdimarsson, H., Turrell, B., Steur, L. d., Quadfasel, D., ... Berx, B. (2019). Arctic Mediterranean exchanges: a consistent volume budget and trends in transports from two decades of observations. *Ocean Science*, *15*(2), 379–399.

Pillar, H. R., Heimbach, P., Johnson, H. L., & Marshall, D. P. (2016). Dynamical Attribution of Recent Variability in Atlantic Overturning. *Journal of Climate*, *29*(9), 3339–3352. doi: 10.1175/JCLI-D-15-0727.1

Pillar, H. R., Johnson, H. L., Marshall, D. P., Heimbach, P., & Takao, S. (2018). Impacts of Atmospheric Reanalysis Uncertainty on Atlantic Overturning Estimates at 25°N. *Journal of Climate*, *31*(21), 8719–8744. doi: 10.1175/JCLI-D-18-0241.1

Ritz, S. P., Stocker, T. F., Grimalt, J. O., Menviel, L., & Timmermann, A. (2013). Estimated strength of the Atlantic overturning circulation during the last deglaciation. *Nature Geoscience*, *6*(3), 208–212. doi: 10.1038/ngeo1723

Roberts, C. D., & Palmer, M. D. (2012). Detectability of changes to the Atlantic meridional overturning circulation in the Hadley Centre Climate Models. *Climate Dynamics*, *39*(9), 2533–2546. doi: 10.1007/s00382-012-1306-3

Schauer, U., & Beszczynska-Möller, A. (2009). Problems with estimation and interpretation of oceanic heat transport - conceptual remarks for the case of Fram Strait in the Arctic Ocean. *Ocean Science*, *5*(4), 487–494. doi: https://doi.org/10.5194/os-5-487-2009

Smith, T., & Heimbach, P. (2019). Atmospheric origins of variability in the South Atlantic meridional overturning circulation. *Journal of Climate*, *32*(5), 1483-1500. doi: 10.1175/JCLI-D-18-0311.1

Tarantola, A. (2005). *Inverse Problem Theory and Methods for Model Parameter Estimation*. Society for Industrial and Applied Mathematics.

Thacker, W. C. (1989). The role of the Hessian matrix in fitting models to measurements. *Journal of Geophysical Research: Oceans*, *94*(C5), 6177–6196. doi: 10.1029/JC094iC05p06177

Thornalley, D. J. R., Oppo, D. W., Ortega, P., Robson, J. I., Brierley, C. M., Davis, R., ... Keigwin, L. D. (2018). Anomalously weak Labrador Sea convection and Atlantic overturning during the past 150 years. *Nature*, *556*(7700), 227–230. doi: 10.1038/s41586-018-0007-4

Vellinga, M., & Wood, R. A. (2004). Timely detection of anthropogenic change in the Atlantic meridional overturning circulation. *Geophysical Research Letters*, *31*(14). doi: 10.1029/2004GL020306

Verdy, A., Mazloff, M. R., Cornuelle, B. D., & Kim, S. Y. (2013). Wind-Driven Sea Level Variability on the California Coast: An Adjoint Sensitivity Analysis. *Journal of Physical Oceanography*, *44*(1), 297–318. doi: 10.1175/JPO-D-13-018.1

Weller, R. A., Baker, D. J., Glackin, M. M., Roberts, S. J., Schmitt, R. W., Twigg, E. S., & Vimont, D. J. (2019). The Challenge of Sustaining Ocean Observations. *Frontiers in Marine Science*, *6*. doi: 10.3389/fmars.2019.00105

Wunsch, C. (1996). *The Ocean Circulation Inverse Problem*. Cambridge: Cambridge University Press.

Zhang, R. (2007). Anticorrelated multidecadal variations between surface and subsurface tropical North Atlantic. *Geophysical Research Letters*, *34*(12). doi: 10.1029/2007GL030225

Zhang, R. (2008). Coherent surface-subsurface fingerprint of the Atlantic meridional overturning circulation. *Geophysical Research Letters*, *35*(20), L20705. doi: 10.1029/2008GL035463

Zhang, X., Prange, M., Merkel, U., & Schulz, M. (2015). Spatial fingerprint and magnitude of changes in the Atlantic meridional overturning circulation during marine isotope stage 3. *Geophysical Research Letters*, *42*(6), 2014GL063003. doi: 10.1002/2014GL063003